# Polytechnic of Torino

Master of Science in

*Nanotechnologies for ICTs*

## Master degree thesis

*Actuation in microchannels through*

*surface acoustic waves*


Relators:

Dr. Ricciardi Carlo

Dr. Rochus Veronique

Eng. Billen Margo

Eng. Jones Ben

Candidate:

Pagotto Alberto

# Contents

# Chapter 1

# Introduction

Although ultrasound is widely used in biomedical imaging, acoustic manipulation of fluids and particles on the micro to nanoscale is still at research level. Acoustic streaming represents one of the very few inertial phenomena that may play a significant role in microfluidic devices.
The goal of this Master thesis is to analyze a phoenomenon called *acoustic streaming*, which is generated by a nonlinear acoustic field with a finite amplitude propagating in a viscid[1] fluid [1]. The acoustic field is radiated by an InterDigitated Transducer (IDT), which creates a Surface Acoustic Wave (SAW) propagating at the surface of a piezoelectric layer. Other ways of exciting acoustic streaming are possible, as it is reported in the following in this chapter.
In particular first it is presented a general overview of the phoenomenon and its current applications.
In chapter 2 the fundamental mathematical models are detailed, dedicating high focus on the analytical description of surface acoustic waves (SAW) and how the non-linearities of acoustic streaming are taken into account.
The third chapter shows the results of numerical simulations aimed to study how the geometrical properties of the piezoelectric substrate, and the operating frequency, affect the characteristics of SAW.
The outcomes of FEA (Finite Element Analysis) simulations of acoustic streaming are discussed in chapter 4. In particular, it has been decided to limit the study to 2D cases and briefly describe how a 3D analysis should be carried out.
The final chapter presents the general conclusions based on the previous chapters, and make suggestions for interesting future work.

## 1.1 Interdigitated transducers and SAW

SAW devices are widely in MEMs applications because of the great capability they offer in controlling and processing electrical signals[2]. First reported by White and Voltmer in 1965 [3], an interdigitated transducer

[1]Referred to a fluid whose viscosity is non-zero.

(IDT) is "a device that consists in two interlocking comb-like arrays of metallic electrodes deposited on the surface of a piezoelectric substrate to form a periodic alternating pattern"[4], as displayed in fig. 1.1.

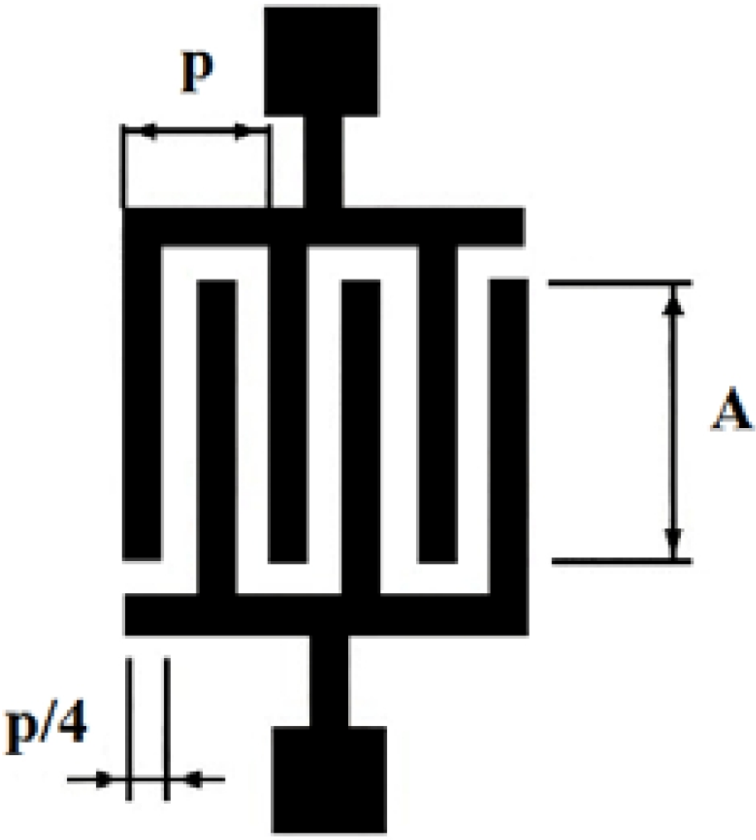


Figure 1.1: Abstract scheme of three couples of electrodes. In this $p$ is the periodicity of the device, and A is the *aperture* of the electrodes[4].

Before discussing the technical aspects, it is fundamental to clarify two terms:

- *interdigitated* refers to a "digit-like (or finger-like) periodic pattern of parallel in-plane electrodes used to build up the capacitance associated with the electric fields that penetrate into the material sample"[5];
- *wavelength* could refer to the radiation wavelength of electromagnetic waves (equal to $\frac{c}{f}$, with $c$ being the speed of light and $f$ the operating frequency), or to the spatial wavelength of a geometrical structure (the distance between the centerlines of the adjacent fingers belonging to the same electrode, indicated in fig. 1.1 as $p$)[5].

One of the combs is connected to ground, while the other one is used to propagate an electrical signal: the spatially periodic electric field produces a corresponding periodic mechanical strain pattern by piezoelectric effect (this phenomenon will be mathematically discussed in section 2). It results

in two surface acoustic waves radiating towards both the directions and orthogonally to the electrodes [6].
Interdigitated transducers are proven to better operate when the wavelength $\lambda$ of the radiated SAW matches the transducer periodicity $p$, and so when the working frequency is $f = \frac{c}{p}$.
Interdigitated transducers are worth for the generation of surface acoustic waves (SAW), which are acoustic waves travelling along the surface of an elastic material.
It is possible to distinguish mostly four different types of SAW:

- **Lamb waves**, displayed in fig. 1.2, travelling in elastic plates

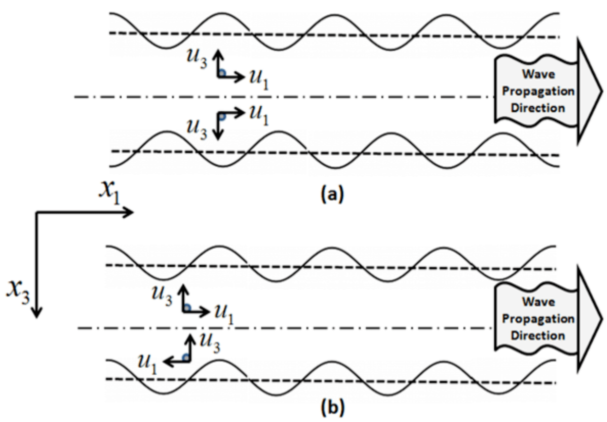


Figure 1.2: Abstract drawing of Lamb waves: (a) simmetric mode (b) antysimmetric mode[7]

- **Love waves**, which are "horizontally polarized shear waves guided by a thin elastic layer set on another elastic solid substrate"[8]. They are shown in fig. 1.3

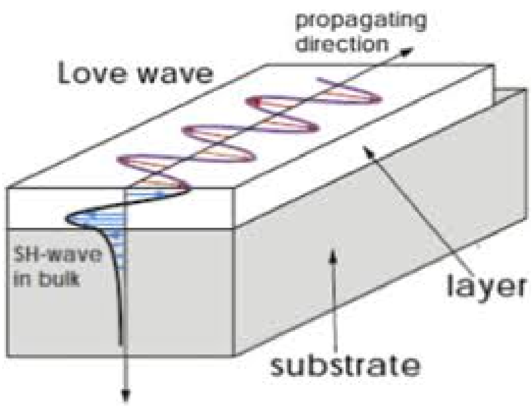


Figure 1.3: Abstract drawing of Love waves[9]

- **Stoneley waves**, travelling along solid-solid interfaces;

- **Scholte waves**, travelling along solid-fluid interfaces;
- **Rayleigh waves**, travelling along vacuum-solid interfaces

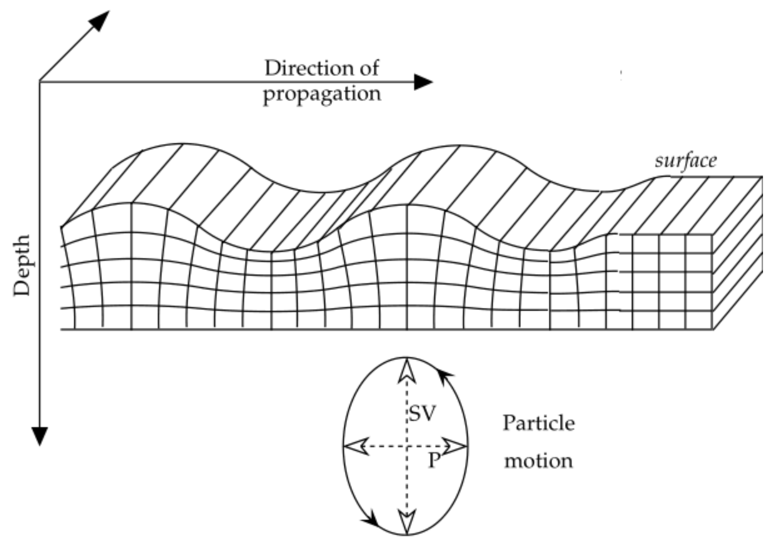


Figure 1.4: Abstract drawing of a Rayleigh wave. $P$ indicates the particle movement generating p-waves (transverse waves), while $SV$ refers to the propagation of s-waves (longitudinal waves) [10]

Moreover, also **pseudo-surface waves** should be considered: they appear in certain crystals when, because of anisotropy, the Rayleigh wave velocity is greater than that of one of the bulk transverse waves[11].
As much as concerns this Master thesis, only Rayleigh waves are taken into account (it can be shown that a Lamb wave transforms into a Rayleigh wave as the thickness of the substrate increases with respect to the wave amplitude[12]).
Rayleigh waves on a solid are similar to surface waves on a liquid, in that particle motion is elliptical[13], as pictured in fig. 1.4. This peculiarity is proven in chapter 2, where full mathematical models are developed.
However, there are differences in direction and restoring forces: in solids their nature is elastic, while in liquids it is gravitational and linked to surface tension[13].
An interesting aspect of SAWs is the propagation speed across the medium, which is lower than the counterpart BAW speed of sound, so causing the wave and its energy to be trapped at the surface[14]. Moreover, "their strong fluid-structural coupling allows to the presence of most of the energy adjacent to the interface, which is responsible for extreme accelerations". Indeed, if it considered the acoustic velocity to be 1m/s, an operating frequency of 10MHz causes the accelation to be $\approx 10^7$m/s$^2$: "SAW-based microfluidics permits the delivery of a complete microfluidics solution at the microscale (sample preparation, analyte detection...), which is essential for lab-on-chip devices"[14].

Most of the IDT device generate acoustic waves towards two opposite directions, perpendicularly to the upper piezoelectric surface.
When an acoustic wave propagates on the surface through an IDT's periodic structure, it is partially reflected at each finger. Depending on the operating frequency of the acoustic wave, the reflected parts interfere constructively or destructively. Generally these reflections are very small and therefore, in the following analysis the effect of the reflections is discarded and it is assumed that a surface wave propagates though each IDT only once[2].
They reveal to be fundamental when designing **single-phase unidirectional transducers** (SPUDTs), "a class of UDTs able to overcome the bidirectionality issue without occupying any additional substrate space and are easily fabricated"[15]. In this case, "internal mechanical reflections are included in order to cancel the effect of the regenerated reflections at one of the acoustic ports (forward or backward), so that the net reflection coefficient is made null in the pass band if the device is properly matched"[9].
The associated drawbacks are a reduction in total SAW energy, and a resulting lower SAW generation efficiency[9].

## 1.2 Acoustic streaming working principles

As previously said, acoustic streaming is the "steady flow of a fluid that is caused by non-linear effects due to the propagation of sound through that fluid", as shown by Rayleigh (1884)[16]. Small feature dimensions generally do not allow flow velocities to be high enough[17]: the reason could be introduced by using Reynolds number

$$\mathrm{Re} = \frac{f_i}{f_v} = \frac{\rho_f U_0 L_0}{\mu} \tag{1.1}$$

where $f_i$ and $f_v$ are the the inertial and viscous forces respectively, $\rho_f$ is the density of the fluid, $U_0$ the associated velocity and $L_0$ the length scale. Since in microfluidics $L_0$ is typically small (typical channel sizes range from 1 to 100 $\mu$m), with typical velocities of 0.1 $\mu$m/s–1mm/s the Reynolds numbers range between $\mathcal{O}(10^{-7})$ and $\mathcal{O}(1)$[18]. So it is clear that viscous forces play a significant role with respect to inertial forces, thus limiting the flow magnitudes.
Acoustic streaming is particularly observable in two famous device: **Kundt's tube** and **Chladni's plate**.
As pictured in fig. 1.5, Kundt's tube is a *horizontal glass cylinder containing air and a small amount of lycopodium powder*[19] (used to make sound waves visible). Sound waves are stimulated in the tube of air, which then generates nodes and antinodes of longitudinal oscillatory speed $U_0$: the lycopodium particles at the bottom of the channel are moved by the streaming phenomenon in the direction of decreasing $|U_0|$[19].

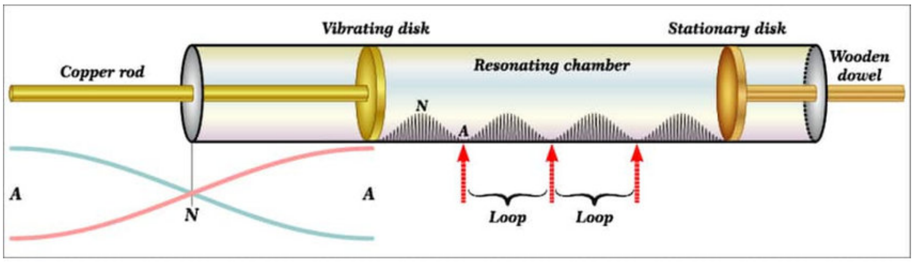


Figure 1.5: Physical scheme of system Kundt's tube, where A indicates the position of the antinodes and N the position of the nodes [20]

Chladni's plate (fig. 1.6) is a *horizontal metal plate clamped at its centre and sprinkled with lycopodium powder, in which a variety of transverse standing waves may be excited*[19]. "Vertical displacement of the plate's surface drives oscillatory air currents, but it is the horizontal component of the air's oscillatory motion which gives rise to acoustic streaming"[19].

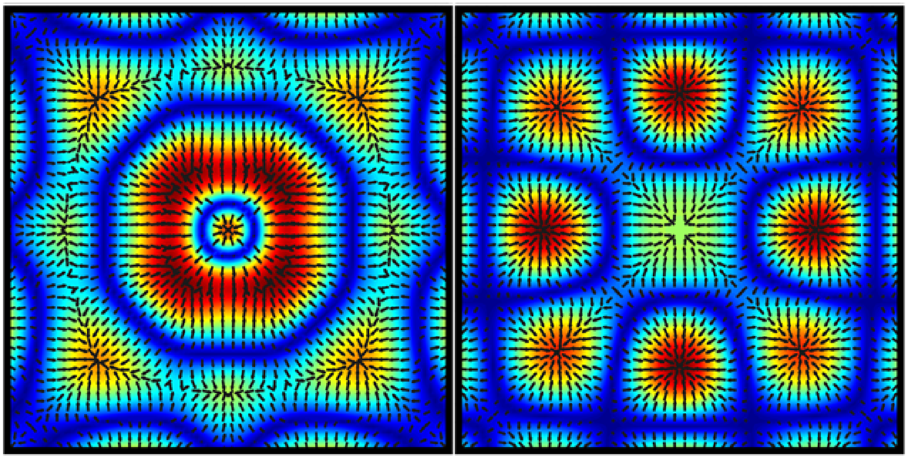

Figure 1.6: Theoretical force patterns for an underwater Chladni's plate at two different frequencies[21]

In general, acoustic streaming can be observed in three different situations, which are detailed in the following.

### 1.2.1 Bulk acoustic streaming

Bulk acoustic streaming is known as *Eckart streaming* and manifests over length scales greater than one sound wavelength: if the channel is small then one wavelength, it could be prevented from appearing[1].
In the bulk of the fluid, during propagation, dissipation causes acoustic waves to decay over an attenuation length $\beta(\omega)^{-1}$, resulting in an oscillatory velocity field (according to Stokes law of sound attenuation) given by eq.

1.2

$$\begin{cases} u_1 & = U_0 e^{-\beta z} e^{i\omega t} \hat{z} \\ \beta(\omega) & = \frac{(\frac{4}{3}\mu + \mu_b)\omega^2}{2\rho_F c_F^3} \end{cases} \tag{1.2}$$

where $\rho_F$ is the density of the fluid, $c_F$ speed on sound in the fluid, $\omega$ the pulsation, $\mu$ and $\mu_b$ the dynamic and bulk viscosities of the fluid.
"The oscillation amplitude of a fluid particle decreases as it moves away from the source, and increases as it moves towards: oscillating fluid particles thus constantly impart momentum to the fluid, driving a secondary streaming flow away from the acoustic source"[18].
In air this phenomenon is known as *quartz wind*[22], and can be exploited to drive microfluidic flows through an acoustic plane wave along a microchannel of length $L \geq \beta^{-1}(\omega)$.

### 1.2.2 Boundary acoustic streaming

Boundary acoustic streaming occurs near **solid boundaries**, where an oscillatory flow must vanish due to the no-slip condition. In unsteady viscous flows, vorticity effects are confined by a layer named *Stokes boundary layer* given by eq. 1.3

$$\delta_V = \sqrt{\frac{2\mu}{\rho\omega}} \tag{1.3}$$

with irrotational flow outside of the Stokes (viscous) layer[18]. It is necessary to distinguish two mechanisms of streaming:

- *Schlichting streaming*, which is caused by viscous attenuation and confined withing the viscous layer;
- *Rayleigh streaming*, which is induced by the streaming in the Stokes layer and presents a vortical pattern[14].

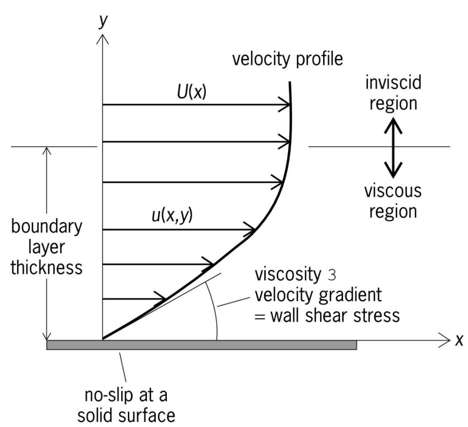


Figure 1.7: Typical laminar boundary-layer velocity profile[23]

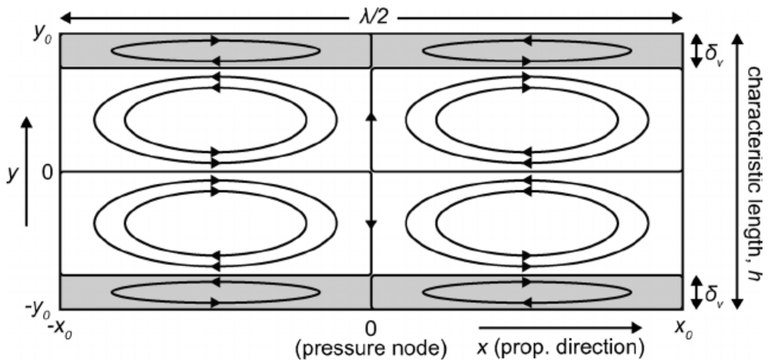


Figure 1.8: A system of inner (Schlichting) streaming within the viscous boundary layer of thickness (gray areas) and outer (Rayleigh) streaming vorticies in a channel with a standing wave propagating along x-direction[24]

### 1.2.3 Cavitation streaming

**Bubbles** subjected to acoustic waves expand and contract as the local pressure varies[18]. Bubble shape and fluid oscillations are rectified to give rise to the so-called *cavitation microstreaming*[25].

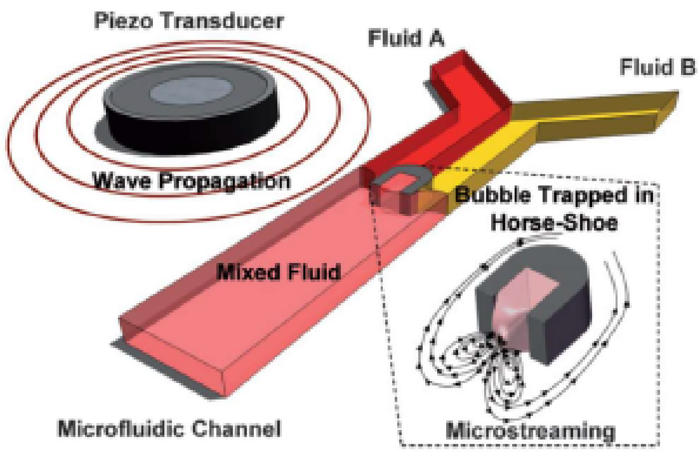


Figure 1.9: Schematic representation of horse-shoe piezo transducer setup in a microfluidic system to induce mixing and [26]

## 1.3 Acoustic-streaming pumps

The acoustic streaming effect has been proposed to improve **mixing**[27], **agitation**[28] and **pumping** in open microfluidic systems, which were or chemically alterated to confine the liquid, or cut by lasers directly into the substrate to guide the fluid[29].
The following section will focus on the different pumping mechanisms, of which some will be evaluated in more detatil in the following chapters.

Micropumps represent a fundamental component to control flow in microfluidic systems. They are commonly divided into two main categories[30]:

- **mechanical** pumps, which "take advantage of moving parts such as check valves, oscillating membranes, or turbines for delivering a constant fluid volume in each pump cycle, resulting in a pulsating flow";
- **non-mechanical** pumps, which "pump the fluid by turning a specific kind of energy into kinetic, delivering a continous flow thanks to the direct interaction with the working fluid through electrical, magnetic or chemical means"[31].

Acoustic-based pumps belong to the second group, and in particular SAW-based pumps have the advantages of controlling the fluid **without any external fluid connection** and **high flow rates**.
In the following a device[32] is presented: it is based on the SAW-induced counterflow mechanism, where SAW propagation and fluid actuation are oppositely directed[33] (as displayed in fig. 1.10).

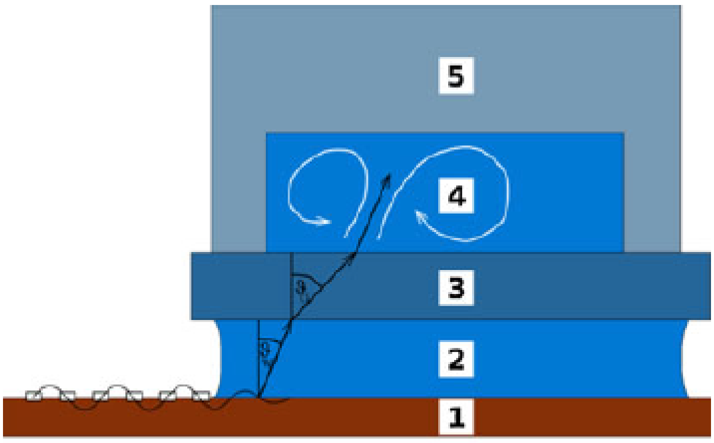


Figure 1.10: Scheme of the device a closed chamber where the streaming is induced by SAW[32]

The working principle of such a device could be devided into five steps, each one corresponding to a specific number in fig. 1.10:

1. A sinusoidal voltage is applied to IDTs to generate SAW propagating towards the channel. According to Snell's law, once the wave has reached the channel, it is refracted as a longitudinal wave into water with an angle equal to

$$\theta_f = \sin^{-1}\left(\frac{c_f}{c_{SAW}} \cdot \sin\theta_{inc}\right) \approx 22° \tag{1.4}$$

$$\alpha = \frac{1}{l_a} = \frac{\rho_F v_F}{\rho_{SAW} v_{SAW} \lambda_{SAW}} \tag{1.5}$$

where $\theta_f$ is the refracted angle, $\alpha$ the attenuation coefficient of the leaky surface acoustic wave, $l_a$ is the attenuation length, $c_f$ and $c_{SAW}$ the speed of sound in the fluid and along the piezoelectric layer, $\rho_f$ and $\rho_{SAW}$ are the densities of the fluid and the piezoelectric layer respectively, $\lambda_{SAW}$ the substrate wavelength and $\theta_{inc}$ the incidence angle. It is worth to notice that even at this stage two loss sources are relevant: -0.28dB because of IDT impedance mismatch, and -3.01dB because of the backward SAW (not providing any contribution).

2. The longitudinal acoustic wave passes through the $150\mu m$-thick water layer and is subsequently refracted at the water-glass interface as a transversal wave at a Rayleigh angle of

$$\begin{cases} \theta_{glass,trans} &= \sin^{-1}(\frac{c_{glass,trans}}{c_f} \cdot \sin\theta_f) &= 55.1° \\ c_{glass,trans} &= 3280\mathrm{m/s} \end{cases} \tag{1.6}$$

where $\theta_{glass,trans}$ is the refracted angle of the transversal wave, and $c_{glass,trans}$ is the speed of a transversal acoustic wave travelling through glass.
The reason for such a phenomenon is related to the critical angle of the longitudinal wave, which is lower than the incidence angle as proved by eq. 1.7

$$\begin{cases} \theta_{crit,long} &= \sin^{-1}(\frac{c_f}{c_{glass,long}}) &= 15.4° < 22° \\ c_{glass,long} &= 5640\mathrm{m/s} \end{cases} \tag{1.7}$$

where $\theta_{glass,long}$ is the refracted angle of the longitudinal acoustic wave, and $c_{glass,long}$ is the speed of a longitudinal acoustic wave travelling through glass.
The attenuation through water (dependent of frequency) is equal to -0.53dB (with $l_a = 1.24mm$), while the transmission at water-glass interface causes an attenuation of -3.64dB.

3. At glass-water interface, the transverse wave is refracted and both a longitudinal and a transverse components are excited. However, because of the critical angle, only the longitudinal one is transmitted. The transmission at glass-water interface causes an attenuation of -3.64dB.

4. The wave is refracted again, enters the water-filled channel and transfers momentum to the liquid, causing acoustic streaming

$$\begin{cases} u_{1,x} &= U_{0,x} \cdot e^{-x/l_a} \cos(k_x x - \omega t) \\ F_x &= \frac{1}{2}\rho_F u_{1x} \cdot \frac{du_{1x}}{dx} &= -\frac{\rho_0 U_{0,x}^2}{l_a} e^{-2x/l_a} \end{cases} \tag{1.8}$$

where $U_{0,x}$ and $F_x$ are the amplitude of the acoustic field and the resulting force along x-direction.

Hagen-Poiseuille flow equations 1.9 describe the velocity profile of laminar flow in rectangular channels as

$$\begin{cases} u(y,z) &= \frac{4G}{\mu W}\sum_{n=1}^{\infty}\frac{(-1)^{n+1}}{\beta_n^3}\left[1-\frac{\cosh(\beta_n z)}{\cosh(\beta_n H/2)}\right]\cos(\beta_n y) \\ Q &= \frac{8GH}{\mu W}\sum_{n=1}^{\infty}\frac{1}{\beta_n^4}\left[1-\frac{2}{\beta_n H}\tanh\left(\frac{\beta_n H}{2}\right)\right] \\ \beta_n &= (2n-1)\frac{\pi}{W} \end{cases} \tag{1.9}$$

where $u$ is the velocity of fluid perpendicularly to the plane, $Q$ is the flow rate, $G$ is the linear pressure gradient, $\mu$ the dynamic viscosity, $W$ and $H$ the width and the height of the channel.
Fig. 1.11 shows the velocity profile of a water channel ($\mu = 0.89$mPa·s) when $W = H = 1$mm, $G = 28.5$Pa/m: according to eq. 1.9, the velocity profile is maximum at the centre of the channel ($z = 0$), and minimum at the sides ($z = \pm W/2$).

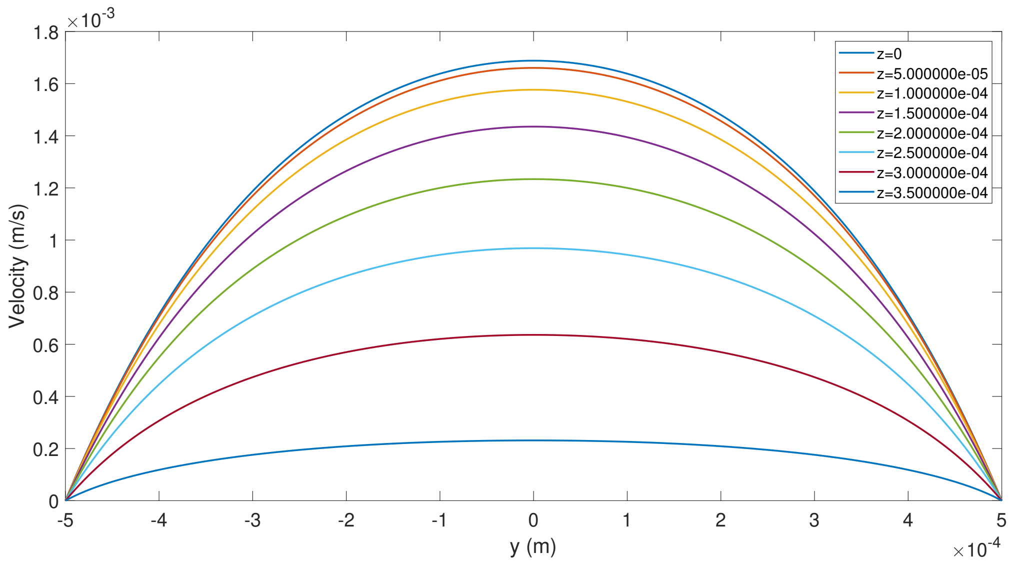


Figure 1.11: Velocity profile of water laminar flowing

5. The acoustic waves couple into the PDMS layer on top, where it is further dampened.

# Chapter 2

# Mathematical development

This chapter is the dedicated the analysis of the existent mathematical models to describe the two most important physical phenomena involved in the device studied in this Master thesis: **piezoelectricity** and **acoustic streaming**. The former is investigated by following two different paths, while the latter is studied by applying the most known method to deal with acoustophoretic phenomena.
However, it is pointed out that a comparison between these models and the FEM (Finite Element Models) in chapters 3 and 4 results to be difficult: it is due to the complexity of the resulting differential equations, in particular for the microfluidics section.

## 2.1 Piezoelectricity

Piezoelectricity is the ability of some materials (notably crystals and certain ceramics) to generate an electric charge in response to applied mechanical stress. Viceversa, if the material is not short-circuited, the applied charge induces a voltage across the material [34].
The piezoelectric effect is reversible, so piezoelectric materials always exhibit both:

- the **direct** piezoelectric effect, consisting in the production of electricity when the material is stressed from the external;
- the **converse** (or **inverse**) piezoelectric effect, that is the production of stress and/or strain when an electric field is applied.

In order to describe the piezoelectric phenomenon, first consider two sets of equation:

- eq. 2.1 describing the **electrostatics** contribution.

$$\begin{cases} \nabla \cdot \boldsymbol{D} = q \\ \boldsymbol{E} = -\nabla\phi \\ \boldsymbol{D} = \boldsymbol{e} : \boldsymbol{S} + \boldsymbol{\epsilon} \cdot \boldsymbol{E} \end{cases} \tag{2.1}$$

where $q$ is the body electric charge per unit volume, $\phi$ is the applied electric potential, and $\boldsymbol{e} : \boldsymbol{S}$ is the notation for a double-dot product[35].

- eq. 2.2 describing the **elastodynamics** contribution.

$$\begin{cases} \rho\ddot{\boldsymbol{u}} &= \nabla \cdot \boldsymbol{T} + \boldsymbol{f} \\ \boldsymbol{S} &= \frac{1}{2}[\nabla\boldsymbol{u} + (\nabla\boldsymbol{u})^T] \\ \boldsymbol{T} &= \boldsymbol{c} : \boldsymbol{S} - \boldsymbol{e}^T \cdot \boldsymbol{E} \end{cases} \tag{2.2}$$

  where $\boldsymbol{f}$ is the body force vector.

In case of sourceless mechanical and electrical systems ($q = 0$ and $\boldsymbol{f} = 0$), equations for electrostatics and elastodynamics are rewritable in Cartesian coordinates respectively as eq. 2.3 and 2.4.

$$\begin{cases} E_i &= -\frac{\partial\phi}{\partial x_i} \\ D_i &= \sum_j\sum_k e_{ijk}S_{jk} + \sum_j \epsilon^S_{ij}E_j \\ \sum_{i=1}^3 \frac{\partial D_i}{\partial x_i} &= 0 \end{cases} \tag{2.3}$$

$$\begin{cases} \rho\frac{\partial^2 u_i}{\partial t^2} &= \sum_{j=1}^3 \frac{\partial T_{ij}}{\partial x_j} \\ S_{ij} &= \frac{1}{2}(\frac{\partial u_i}{\partial x_j} + \frac{\partial u_j}{\partial x_i}) \\ T_{ij} &= \sum_k\sum_l c^E_{ijkl}S_{kl} - \sum_k e_{kij}E_k \end{cases} \tag{2.4}$$

If proper substitutions are applied, eq. 2.5 and 2.6 are obtainable.

$$\sum_{i=1}\sum_{j=1}\left(\sum_{k=1} e_{ijk}\frac{\partial^2 u_j}{\partial x_i \partial x_k} - \epsilon^S_{ij}\frac{\partial^2\phi}{\partial x_i\partial x_j}\right) = 0 \tag{2.5}$$

$$\rho\frac{\partial^2 u_i}{\partial t^2} = \sum_j\sum_k\left(e_{kij}\frac{\partial^2\phi}{\partial x_j\partial x_k} + \sum_l \frac{\partial^2 u_k}{\partial x_j \partial x_l}\right) \tag{2.6}$$

## 2.2 Surface acoustic waves

In the following, two approaches to mathematically model surface acoustic waves are proposed. The first one is based on the introduction of two **scalar functions** and does not provide any relation between the applied voltage and the deformation of the elastic solid. The second one is based on the **partial wave method**, but it results to be difficult to handle.
The direction of periodicity is denoted by $x_1$, the surface normal direction by $x_3$, and their perpendicular direction $x_2$ following a right-handed coordinate system[36]. The dimensional extension of electrodes in $x_2$-direction is much larger in comparison to the periodicity. Additionally, a homogeneous material topology is assumed in $x_2$-direction for this analysis.
Instead of performing a full 3D analysis, a model reduction is performed in the geometric domain and the analysis is carried out within the sagittal plane. In order to derive an expression for the resultant electrostatic force, the following assumptions are made of the model and the analysis, as well as simplifications to both are mentioned:

- *the frequency of the induced electric field wave is sufficiently small enough to reasonably assume the electromagnetic coupling effects to be negligible. This means that local perturbations are felt almost instantaneously through out the substrate*[36];

- if $l$ is the largest characteristic dimension of the actuator structure (i.e. $x_2$) and $c$ is the speed of light, *the generated electromagnetic coupling effects can be safely discarded, if the operating frequency of the device is much less than the ratio* $c/l$[36].

### 2.2.1 Method based on scalar functions

The equation of motion for an unbounded isotropic elastic solid in which body forces are absent[13] can be written as

$$\rho\frac{\partial^2 u_1}{\partial t^2} = (\lambda+\mu)\frac{\partial \Delta}{\partial x_1} + \mu\nabla^2 u_1 \tag{2.7}$$

$$\begin{cases} \Delta = \frac{\partial u_1}{\partial x_1} + \frac{\partial u_3}{\partial x_3} \\ \Omega_2 = \frac{\partial u_1}{\partial x_3} - \frac{\partial u_3}{\partial x_1} \end{cases} \tag{2.8}$$

where is $\Delta$ the dilatation, and $\Omega_2$ the rotation in the xz plane.
It is worth to introduce two scalar orthogonal functions $\Phi$ and $\Psi$ so that

$$\begin{cases} \Phi = F(x_3)e^{i(\omega t - kx_1)} \\ \Psi = G(x_3)e^{i(\omega t - kx_1)} \\ F(z) = A_1 e^{-\gamma_L x_3} + A_2 e^{\gamma_L x_3} \\ G(z) = B_1 e^{-\gamma_T x_3} + B_2 e^{\gamma_T x_3} \end{cases} \tag{2.9}$$

where $\omega$ is the operating frequency, $k$ is the wave number, $\gamma_L$ and $\gamma_T$ are two attenuation coefficients, $A_1$, $A_2$, $B_1$ and $B_2$ are the weight coefficients. It is clear that $A_2$ and $B_2$ have to be null to avoid any nonsense physical divergence at the bottom part of the substrate, and so eq. 2.9 reduces to

$$\begin{cases} \Phi = A_1 e^{-\gamma_L x_3} \cdot e^{i(\omega t - kx_1)} \\ \Psi = B_1 e^{-\gamma_T x_3} \cdot e^{i(\omega t - kx_1)} \end{cases} \tag{2.10}$$

If the following condition is assumed

$$\begin{cases} u_1 = \frac{\partial \Phi}{\partial x_1} + \frac{\partial \Psi}{\partial x_3} \\ u_3 = \frac{\partial \Phi}{\partial x_3} - \frac{\partial \Psi}{\partial x_1} \end{cases} \tag{2.11}$$

equation 2.8 reduces to

$$\begin{cases} \Delta = \frac{\partial^2 \Phi}{\partial x_1^2} + \frac{\partial^2 \Phi}{\partial x_3^2} = \nabla^2\Phi \\ \Omega_2 = \frac{\partial^2 \Psi}{\partial x_1^2} + \frac{\partial^2 \Psi}{\partial x_3^2} = \nabla^2\Psi \end{cases} \tag{2.12}$$

By substituting eq. 2.7 into eq. 2.12, it is possible to get

$$\begin{cases} \frac{\partial^2\Phi}{\partial t^2} &= c_L^2\nabla^2\Phi \\ \frac{\partial^2\Psi}{\partial t^2} &= c_T^2\nabla^2\Psi \\ c_L &= \sqrt{\frac{\lambda+2\mu}{\rho}} \\ c_T &= \sqrt{\frac{\mu}{\rho}} \end{cases} \tag{2.13}$$

where $c_L$ and $c_T$ are the longitudinal and transverse velocities respectively. Finally, by expliciting $\Phi$ and $\Psi$ (eq.2.10)

$$\begin{cases} \frac{\partial^2 F(x_3)}{\partial z^2} &= \gamma_L^2 F(x_3) \\ \frac{\partial^2 G(x_3)}{\partial z^2} &= \gamma_T^2 G(x_3) \\ \gamma_L &= \sqrt{k^2-k_L^2} \\ \gamma_T &= \sqrt{k^2-k_T^2} \\ k_L &= \frac{\omega}{c_L} \\ k_T &= \frac{\omega}{c_T} \end{cases} \tag{2.14}$$

where $k > k_T > k_L$.
Stress components $T_{33}$ and $T_{13}$ can be expressed as a function of $\Phi$ and $\Psi$ as shown in eq. 2.15.

$$\begin{cases} T_{33} &= \lambda(S_{11}+S_{33})+2\mu S_{33} &= [(\lambda+2\mu)\gamma_L^2-\lambda k^2]\Phi-2\mu ik\gamma_T\Phi \\ T_{13} &= \mu S_{13} &= \mu[(\gamma_T^2+k^2)\Psi+2ik\gamma_L\Phi] \end{cases} \tag{2.15}$$

In order to get an expression for $k$, it is necessary to impose two boundary conditions on the plane and shear stress components at the free surface (eq. 2.16)

$$\begin{cases} T_{33}(x_3=0) &= [(\lambda+2\mu)\gamma_L^2-\lambda k^2]A_1-2i\mu k\gamma_T B_1 &= 0 \\ T_{13}(x_3=0) &= \mu(\gamma_T^2 B_1+k^2B_1+2ik\gamma_L A_1) &= 0 \end{cases} \tag{2.16}$$

which leads to

$$[(\lambda+2\mu)\gamma_L^2-\lambda k^2](k^2+\gamma_T^2) \ = \ 4\mu k^2\gamma_L\gamma_T \tag{2.17}$$

If substitutions indicated in eq. 2.18 are applied

$$\begin{cases} k_L &= \alpha_1 k_T \\ \alpha_1 &= \sqrt{\frac{\mu}{\lambda+2\mu}} \\ s &= \frac{k_T}{k} \end{cases} \tag{2.18}$$

$6^{th}$-order eq. 2.19 is obtained.

$$s^6-8s^4+(24-16\alpha_1^2)s^2+(16\alpha_1^2-16) \ = \ 0 \tag{2.19}$$

It is clear that eq.2.18 could be reduced to a $3^{rd}$-order one: however, the correspondent analytical solution couldn't be expressed in a simple way, so it is reported the solution proposed by Viktorov[37]

$$s = \frac{0.87 + 1.12\nu}{1 + \nu} \tag{2.20}$$

where $\nu$ is the Poisson ratio of the elastic solid.
By solving eq. 2.16 it is possible to get $B_1$ as a function of $A_1$, and so rewrite eq. 2.11 into

$$\begin{cases} u_1 = A_1 k(e^{-\gamma_L x_3} - 2\frac{\gamma_L \gamma_T}{k^2+\gamma_T^2} e^{-\gamma_T x_3}) \sin(\omega t - k x_1) \\ u_3 = -A_1 \gamma_L (e^{-\gamma_L x_3} - \frac{2k^2}{k^2+\gamma_T^2} e^{-\gamma_T x_3}) \cos(\omega t - k x_1) \end{cases} \tag{2.21}$$

which clearly highlights the fact that particles move following elliptical traces.
The above analysis assumes the absence of any load over the free surface (*unloaded case*), for which it is valid

$$4k^2 \gamma_L \gamma_T - (k^2 + \gamma_T^2)^2 = 0 \tag{2.22}$$

As the impedance of the fluid rises from zero (*loaded case*), the wave behaves less like a *pure* Rayleigh wave and transforms into a *leaky* one[13]: the above equation turns into

$$\begin{cases} 4k^2 \gamma_L \gamma_T - (k^2 + \gamma_T^2)^2 = i\frac{\rho_F}{\rho_R} \frac{\gamma_L k_T^4}{\sqrt{k_F^2 - k^2}} \\ c_F < c_R \rightarrow k_F > k \end{cases} \tag{2.23}$$

where $\rho_F$ is the liquid density, $c_F$ is the speed of sound in the fluid, $\rho_R$ is the density of the elastic material and $c_R$ is the Rayleigh velocity.
It can be proved that one of the solution of eq. 2.23 corresponds to a wave radiating in the fluid with an angle given by eq. 1.6. The leaky SAW, propagating at the solid-liquid interface, is attenuated by a coefficient given by

$$\alpha = \frac{\rho_F c_F}{\rho_R c_R \lambda_R} = \frac{\rho_F c_F f}{\rho_R c_R^2} \tag{2.24}$$

### 2.2.2 Method based on partial waves

It is the most precise method to solve equations for Surface Acoustic Waves on anisotropic substrates like piezoelectric ones"[36]. It consists in expressing each displacement component and the electric potential as

$$\begin{cases} u_j^m(x_1, x_3, t) = \alpha_j^m e^{ikb^m x_3} \cdot e^{ik(x_1 - vt)} \\ \phi^m(x_1, x_3, t) = \alpha_4^m e^{ikb^m x_3} \cdot e^{ik(x_1 - vt)} \\ m \in \{1, 2, 3, 4\} \\ j \in \{1, 2, 3\} \end{cases} \tag{2.25}$$

where the $\alpha_j^m$ values are linear coefficients that depend on the decaying constant $b_m$, $k$ is the wave vector and $v$ is the phase velocity.
By substituting the expressions of eq. 2.25 into 2.5 and 2.6, it is possible to get an homogeneous linear system in the form

$$\overline{\overline{M}} \cdot \overline{\alpha} \; = \; 0 \tag{2.26}$$

$$\overline{\overline{M}} \; = \; \begin{pmatrix} m_{11} - \rho v^2 & m_{12} & m_{13} & m_{14} \\ m_{12} & m_{22} - \rho v^2 & m_{23} & m_{24} \\ m_{13} & m_{23} & m_{33} - \rho v^2 & m_{34} \\ m_{14} & m_{24} & m_{34} & m_{44} \end{pmatrix} \quad \overline{\alpha} \; = \; \begin{pmatrix} \alpha_1 \\ \alpha_2 \\ \alpha_3 \\ \alpha_4 \end{pmatrix} \tag{2.27}$$

where

$$\begin{cases} m_{11} \; = \; c_{11}^E + c_{55}^E b^2 \\ m_{12} \; = \; (c_{14}^E + c_{56}^E) b \\ m_{13} \; = \; (c_{13}^E + c_{55}^E) b \\ m_{14} \; = \; (e_{13} + e_{51}) b \\ m_{22} \; = \; c_{66}^E + c_{44}^E b^2 \\ m_{23} \; = \; c_{56}^E + c_{34}^E b^2 \\ m_{24} \; = \; e_{61} + e_{43} b^2 \\ m_{33} \; = \; c_{55}^E + c_{33}^E b^2 \\ m_{34} \; = \; e_{51} + e_{33} b^2 \\ m_{44} \; = \; \epsilon_{11} + \epsilon_{33} b^2 \end{cases} \tag{2.28}$$

In order to determine the non-trivial solution ($\overline{\alpha} = 0$), it is necessary to impose

$$|\overline{\overline{M}}| \; = \; 0 \tag{2.29}$$

Eq. 2.29 is reducible to an eighth-order equation in the decaying constant $b$. However, the resulting roots are either purely real or complex conjugate pairs: only the ones with positive imaginary part are accepted to be consistent with the physical meaning of wave propagation in piezoelectric media. There are four such roots for $b$ (denoted as $\mathrm{b}_m$), and for each such value

$$\{b^m\} \Leftrightarrow \{\overline{\alpha}^m\} \tag{2.30}$$

A general solution is the obtained as a linear combination of partial waves, as shown in eq. 2.31

$$\begin{cases} u_j(x_1, x_3, t) \; = \; \left[ \sum_{m=1}^4 C_m \cdot \alpha_j^m e^{ikb^m x_3} \right] e^{ik(x_1 - vt)} \\ \phi(x_1, x_3, t) \; = \; \left[ \sum_{m=1}^4 C_m \cdot \alpha_4^m e^{ikb^m x_3} \right] e^{ik(x_1 - vt)} \end{cases} \tag{2.31}$$

where $C_m$ are weighting coefficients chosen to satisfy the mechanical and electrical boundary conditions at the surface of the piezolectric substrate specific to this model.
Since the mass of the IDTs is considered to be negligible for simplicity,

mechanical force acting on the substrate can be discarded. Hence the surface is considered to be mechanically free, and so the boundary condition

$$\sum_{j=1}^{3} T_{3j}(z=0) \;=\; 0 \tag{2.32}$$

is applyable.
Partial wave method allows to clearly distinguish the contribution any involved matrix elements, but at the same time it results difficult to manuanlly handled it: numerical tools are necessary, making a deep analysis less easy to be achieved.

## 2.3 Acoustic-fluidic interface

According to Navier-Stokes equations, the mass and momentum balance laws governing the motion of a linear viscous compressible fluid are

$$\frac{\partial \rho}{\partial t} + \nabla \cdot (\rho \boldsymbol{u}) \;=\; 0 \tag{2.33}$$

$$\rho \frac{D\boldsymbol{u}}{Dt} \;=\; -\nabla p + \nabla \cdot \boldsymbol{T} + \boldsymbol{f} \tag{2.34}$$

In particular, left-hand term is known as total derivative and has the following form

$$\rho \frac{D\boldsymbol{u}}{Dt} \;=\; \rho \frac{\partial \boldsymbol{u}}{\partial t} + \rho(\boldsymbol{u} \cdot \nabla)\boldsymbol{u} \tag{2.35}$$

and

$$\nabla \cdot \boldsymbol{T} \;=\; \mu \nabla^2 \boldsymbol{u} + \left(\mu_b + \frac{1}{3}\mu\right) \nabla(\nabla \cdot \boldsymbol{u}) \tag{2.36}$$

where $\rho$ is the fluid density, $\boldsymbol{u}$ the fluid velocity field, p the pressure, $\mu$ the dynamic (or shear) viscosity, $\mu_b$ the bulk viscosity.
The terms are

- $\rho \frac{D\boldsymbol{u}}{Dt}$ is the inertial term. In particular $\rho \frac{\partial \boldsymbol{u}}{\partial t}$ is the acceleration term (null for steady-state flows), while $\rho(\boldsymbol{u} \cdot \nabla)\boldsymbol{u}$ is known as advective term and describes the transport of a fluid by bulk motion. Advection can be visualized by *the transport of ink into a river, where the water's movement itself transports the ink*[38]. If added to a lake without significant bulk water flow, *the ink would simply disperse outwards from its source in a diffusive manner, which is not advection*;

- $-\nabla p$ is the diffusive therm;

- $\nabla \cdot \boldsymbol{T}$ is the viscous term. It is worth to notice that $(\mu_b + \frac{1}{3}\mu)\nabla(\nabla \cdot \boldsymbol{u})$ is strictly related to the compressibility of the fluid. In case of water, this term is almost negligible, and so bulk viscosity results to be less relevant the dynamic one;

- $\boldsymbol{f}$ is an external force acting on the fluid.

Equation 2.34 is rewritable in its adimensional form by fixing

$$\begin{cases} \boldsymbol{u_2'} &= \frac{\boldsymbol{u_2}}{U_0} \\ p_2' &= \frac{p_2}{\rho U_0^2} \\ \nabla' &= L_0 \nabla \\ \frac{\partial}{\partial t'} &= \frac{L_0}{U_0} \cdot \frac{\partial}{\partial t} \end{cases} \tag{2.37}$$

where $U_0$ is the mean velocity of the fluid in the channel and $L_0$ is the length scale.
If body and mass-source terms are neglected, and fluid is assumed not to change volume (divergence equal to zero), it results that

$$\begin{cases} \frac{\partial \boldsymbol{u_2'}}{\partial t'} + \tilde{\nabla} p_2' - \frac{1}{\mathrm{Re}} \cdot \nabla'^2 \boldsymbol{u_2'} &= 0 \\ \mathrm{Re} &= \frac{\mu}{\rho L U} \end{cases} \tag{2.38}$$

The viscous term is relevant for Re $\rightarrow 0$, thus confirming what is introduced in section 1.2. An analytical solution satisfying eq. 2.33 and 2.34 is not straightforward to find, in particular because of the widely separated time scales of the acoustic source and the resulting streaming[39]. In the following it is considered only a situation at steady regime, and not transient. The fluid response can be understood to be comprised of two components:

- a **periodic** component with period equal to the forcing period
- a remainder that can be viewed as being **steady**, generally referred to as the streaming motion.

It has been decided to make advantage of Nyborg's perturbation technique[40], in which $p$, $\rho$ and $\boldsymbol{u}$ are assumed to have the following form

$$\begin{cases} p &= p_0 + \epsilon p_1 + \epsilon^2 p_2 \\ \rho &= \rho_0 + \epsilon \rho_1 + \epsilon^2 \rho_2 \\ \boldsymbol{u} &= \epsilon \boldsymbol{u}_1 + \epsilon^2 \boldsymbol{u}_2 \end{cases} \tag{2.39}$$

where $0^{th}$-order expansion variables provide a background contribution, $1^{st}$-order expansion variables represent sound field, $p_2$, $\rho_2$ and $\boldsymbol{u_2}$ and $2^{nd}$-order expansion variables represent acoustic streaming.
$\epsilon$ is a non-dimensional smallness parameter defining the order of the acoustic response[41], and is typically equal to Mach number Ma (eq. 2.40): it is used to understand if a fluid is describable as an incompressible one (generally Ma<0.3).

$$\mathrm{Ma} = \frac{|\boldsymbol{u_1}|}{c_0} \tag{2.40}$$

It is fundamental to notice that the first-order development is unsufficient to describe a stationary flow since

$$\frac{\omega}{2\pi} \int_{-\frac{\pi}{\omega}}^{\frac{\pi}{\omega}} \cos(\omega t)\, dt = 0 \tag{2.41}$$

For this reason it is fundamental to develop a second-order expansion.
It is worth to notice that background velocity is supposed to be zero, so the flow is generated only by acoustic streaming.

### 2.3.1 Zero-order development

$0^{th}$-order expansion does not provide any significative contribution to the current analysis, since

$$\begin{cases} \frac{\partial \rho_0}{\partial t} = 0 \\ \nabla p_0 = 0 \end{cases} \tag{2.42}$$

### 2.3.2 First-order development

$$\begin{cases} \frac{\partial \rho_1}{\partial t} + \rho_0 \nabla \boldsymbol{u_1} = 0 \\ \rho_0 \frac{\partial \boldsymbol{u_1}}{\partial t} + \nabla p_1 - \mu \nabla^2 \boldsymbol{u_1} - (\mu_b + \frac{1}{3}\mu)\nabla(\nabla \cdot \boldsymbol{u_1}) = 0 \end{cases} \tag{2.43}$$

Since a linear relation between $p_1$ and $\rho_1$ is required, isentropic condition 2.44 is applied

$$p_1 = c_0^2 \rho_1 \tag{2.44}$$

In the following, the contribution of bulk viscosity is neglected.
The first line of eq. 2.43 is derived with respect to time, and the second one with respect to space: equation system 2.45 results.

$$\begin{cases} \frac{\partial^2 \rho_1}{\partial t^2} = -\rho_0 \nabla \cdot \frac{\partial \boldsymbol{u_1}}{\partial t} \\ \rho_0 \nabla \cdot \frac{\partial \boldsymbol{u_1}}{\partial t} = -c_0^2 \nabla \cdot (\nabla p_1) + \mu \nabla \cdot (\nabla^2 \boldsymbol{u_1}) + \frac{1}{3}\mu \nabla \cdot [\nabla(\nabla \cdot \boldsymbol{u_1})] \end{cases} \tag{2.45}$$

As soon as an acoustic soleinodal irrotational field is considered vectorial identities

$$\nabla \cdot (\nabla p_1) = \nabla^2 p_1 \tag{2.46}$$

$$\nabla^2 \boldsymbol{u_1} = \nabla(\nabla \cdot \boldsymbol{u_1}) - \nabla \times \nabla \times \boldsymbol{u_1} \rightarrow \nabla \cdot \nabla^2 \boldsymbol{u_1} = \nabla^2(\nabla \cdot \boldsymbol{u_1}) \tag{2.47}$$

are valid, and so eq. 2.48 is writable.

$$\frac{\partial^2 \rho_1}{\partial t^2} = c_0^2 \nabla^2 \rho_1 - \frac{4}{3}\mu \nabla^2 \left( -\frac{1}{\rho_0} \frac{\partial \rho_1}{\partial t} \right) \tag{2.48}$$

which turns into eq. 2.49 if a harmonic dependence $\frac{\partial}{\partial t} = -i\omega$ is assumed.

$$\nabla^2 \rho_1 + \frac{\omega^2}{c_0^2 (1 - i\omega \frac{4\mu}{3\rho_0 c_0^2})} \rho_1 = 0 \tag{2.49}$$

If only physical entities are assumed to vary only along x-direction because of the form factor of the substrate, the solution of eq. 2.49 is

$$\begin{cases} k_{1,2} = \pm \frac{\omega}{c_0 \cdot \sqrt{1 - i\omega \frac{4\mu}{3\rho_0 c_0^2}}} \approx \pm \frac{\omega}{c_0} \cdot \left( 1 + i \frac{2\mu\omega}{3\rho_0 c_0^2} \right) \approx \pm \frac{\omega}{c_0} \\ \rho_1 = A e^{ik_1 x} + B e^{ik_2 x} \end{cases} \tag{2.50}$$

By substituting eq. 2.50 into eq. 2.43, it results that

$$i\omega\rho_1 = \rho_0 \nabla \cdot \boldsymbol{u_1} \rightarrow \frac{i\omega}{\rho_0 c_0^2} \nabla \rho_1 = \nabla^2 \boldsymbol{u_1} \tag{2.51}$$

whose solution is

$$\rho_0 \omega \boldsymbol{u_1} = -i \nabla p_1 \tag{2.52}$$

In order to verify the correctness of the above mathematical procedure, proper boundary conditions are applied in a numerical simulation [42].
The objective consists in plotting the two members of eq. 2.51: if their graphical representations coincide, it means that the written equations for the first-order expansion are valid.
In particular, fig. 2.1 shows the results for a rectangular tube of water, which is closed at its lateral and top sides, and characterized by the following expresion for the acoustic velocity at its bottom side

$$u_{1y} = u_0 2\pi f \sin{(2\pi \frac{x}{W})} \tag{2.53}$$

where $x$ and $y$ are the horizontal and vertical direction respectively. Table 2.1 reports the geometrical parameters of the channel and the operating frequency.

| **Parameter** | **Symbol** | **Unit** | **Value** |
|---|---|---|---|
| Width | $W$ | m | $10^{-3}$ |
| Height | $H$ | m | $10^{-4}$ |
| Operating frequency | $f$ | kHz | 747.5 |

Table 2.1: Parameters involved in the numerical simulation aimed to verify the correctness of equation 2.51

The results of FEA simulation (carried out by the author of this document by using COMSOL™ 5.5) are reported in fig. 2.1 clearly confirms the correctness of eq. 2.51.

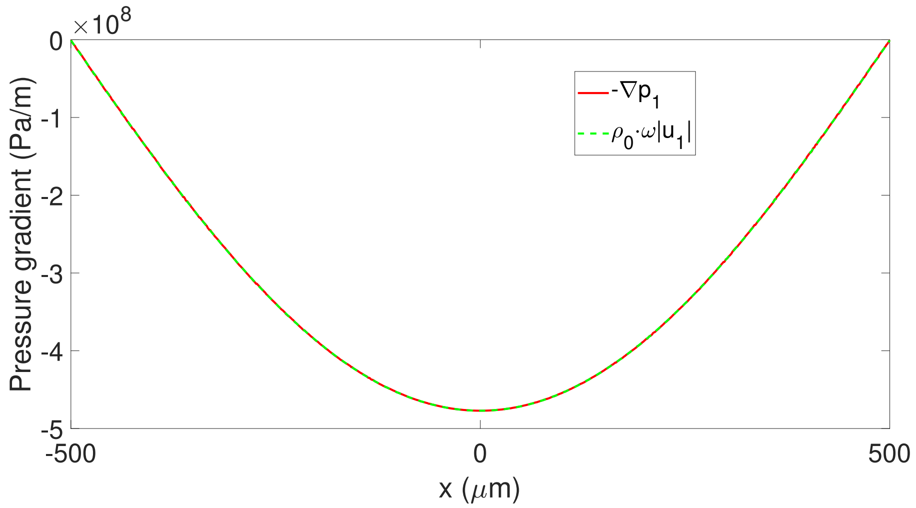


Figure 2.1: Two graphs are displayed, each one corresponding to one of the members of equation 2.51

It is interesting to notice that fig. 2.1 shows the behavior at the bulk of the channel (along a line dividing the channel into two halfs), which does not correspond to the one at the bottom side of the tube. As anticipated in subsection 1.2.2, at the bottom side a *viscous boundary layer* forms: graph 2.2 clearly shows that $u_{1x}$ reaches a regime value at a distance from the wall approximately equal to $2\delta_V$.

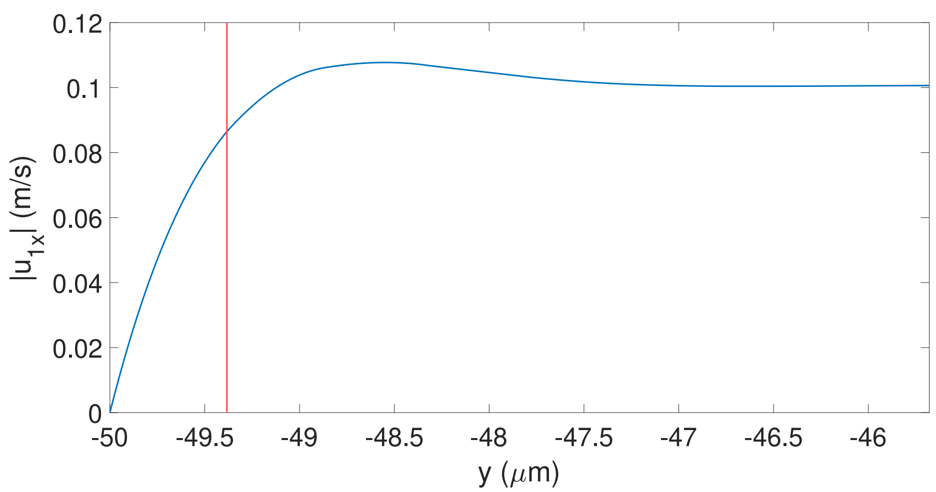


Figure 2.2: In this graph, *red line* is located in order to highlight where the viscous boundary layer is supposed to end

### 2.3.3 Second-order development

$$\begin{cases} \frac{\partial \rho_2}{\partial t} + \rho_0 \nabla \cdot \boldsymbol{u_2} &= -\nabla \cdot (\rho_1 \boldsymbol{u_1}) \\ \rho_0 \frac{\partial \boldsymbol{u_2}}{\partial t} + \nabla p_2 - \mu \nabla^2 \boldsymbol{u_2} - (\mu_b + \frac{1}{3}\mu)\nabla(\nabla \cdot \boldsymbol{u_2}) &= -[\rho_1 \frac{\partial \boldsymbol{u_1}}{\partial t} + \rho_0 (\boldsymbol{u_1} \cdot \nabla)\boldsymbol{u_1}] \end{cases} \tag{2.54}$$

Since the objective is investigating a stationary flow, averaging over time the terms in equations 2.54 results fundamental. Indeed, because of their sinusoidal nature, the time derivative of $p_2$ and $\boldsymbol{u_2}$ do not provide any contribution (eq. 2.55)

$$\begin{cases} \overline{\frac{\partial \rho_2}{\partial t}} &= 0 \\ \overline{\frac{\partial \boldsymbol{u_2}}{\partial t}} &= 0 \end{cases} \tag{2.55}$$

In the following equation, the second term is known as **mass-source term**, while the third one as **volume-force (or body) term**

$$\begin{cases} \nabla \cdot \overline{\rho_1 \boldsymbol{u_1}} &= \frac{1}{2}\mathrm{Re}\{\nabla \cdot (\tilde{\rho_1} \tilde{\boldsymbol{u_1}}^*)\} \\ \overline{\rho_1 \cdot \frac{\partial \boldsymbol{u_1}}{\partial t}} &= \frac{1}{2}\mathrm{Re}\{\tilde{\rho_1}(\frac{\partial \tilde{\boldsymbol{u_1}}}{\partial t})^*\} \\ \rho_0 \overline{\boldsymbol{u_1} \cdot \nabla \boldsymbol{u_1}} &= \frac{\rho_0}{2}\mathrm{Re}\{(\tilde{\boldsymbol{u_1}} \cdot \nabla)\tilde{\boldsymbol{u_1}}^*\} \end{cases} \tag{2.56}$$

where

$$\begin{cases} \rho_1(t) &= \mathrm{Re}\{\tilde{\rho_1} e^{i\omega t}\} \\ \boldsymbol{u_1}(t) &= \mathrm{Re}\{\tilde{\boldsymbol{u_1}} e^{i\omega t}\}. \end{cases} \tag{2.57}$$

It is possible to rewrite eq. 2.54 according to the Cartesian system: the first equation as

$$\rho_0 \left( \frac{\partial u_{2x}}{\partial x} + \frac{\partial u_{2y}}{\partial y} + \frac{\partial u_{2z}}{\partial z} \right) = -\frac{1}{2}\mathrm{Re}\{\tilde{\rho_1} \tilde{\boldsymbol{u_1}}^*\} \tag{2.58}$$

and the second one as a set of three scalar equations (eq. 2.59, 2.60 and 2.61)

$$\frac{\partial p_2}{\partial x} - \mu \left( \frac{\partial^2 u_{2x}}{\partial x^2} + \frac{\partial^2 u_{2x}}{\partial y^2} + \frac{\partial^2 u_{2x}}{\partial z^2} \right) - \left( \mu_b + \frac{1}{3}\mu \right) \cdot \left( \frac{\partial^2 u_{2x}}{\partial x^2} + \frac{\partial^2 u_{2y}}{\partial x \partial y} + \frac{\partial^2 u_{2z}}{\partial x \partial z} \right) = -\frac{1}{2}\mathrm{Re}\left[ i\omega \rho_1 u_{1x} + \rho_0 \left( u_{1x} \frac{\partial u_{1x}}{\partial x} + u_{1y} \frac{\partial u_{1x}}{\partial y} + u_{1z} \frac{\partial u_{1x}}{\partial z} \right) \right] \tag{2.59}$$

$$\frac{\partial p_2}{\partial y} - \mu \left( \frac{\partial^2 u_{2y}}{\partial x^2} + \frac{\partial^2 u_{2y}}{\partial y^2} + \frac{\partial^2 u_{2y}}{\partial z^2} \right) - \left( \mu_b + \frac{1}{3}\mu \right) \cdot \left( \frac{\partial^2 u_{2x}}{\partial y \partial x} + \frac{\partial^2 u_{2y}}{\partial y^2} + \frac{\partial^2 u_{2z}}{\partial y \partial z} \right) = -\frac{1}{2}\mathrm{Re}\left[ i\omega \rho_1 u_{1y} + \rho_0 \left( u_{1x} \frac{\partial u_{1y}}{\partial x} + u_{1y} \frac{\partial u_{1y}}{\partial y} + u_{1z} \frac{\partial u_{1y}}{\partial z} \right) \right] \tag{2.60}$$

$$\frac{\partial p_2}{\partial z} - \mu \left( \frac{\partial^2 u_{2z}}{\partial x^2} + \frac{\partial^2 u_{2z}}{\partial y^2} + \frac{\partial^2 u_{2z}}{\partial z^2} \right) - \left( \mu_b + \frac{1}{3}\mu \right) \cdot \left( \frac{\partial^2 u_{2x}}{\partial z \partial x} + \frac{\partial^2 u_{2y}}{\partial z \partial y} + \frac{\partial^2 u_{2z}}{\partial z^2} \right) = -\frac{1}{2}\mathrm{Re}\left[ i\omega \rho_1 u_{1z} + \rho_0 \left( u_{1x} \frac{\partial u_{1z}}{\partial x} + u_{1y} \frac{\partial u_{1z}}{\partial y} + u_{1z} \frac{\partial u_{1z}}{\partial z} \right) \right] \tag{2.61}$$

With respect to the first-order expansion, the development of the second-order coupled equations results to be of extreme importance, because COMSOL$^{TM}$ does not provide any Multiphysics to couple acoustic and laminar flow phenomena.
For this reason, finer methods to include the mass-source and body force terms are required, as it is described in chapter 4.

# Chapter 3

# Numerical model of SAW

As highlighted by Gupta[43], "it is highly important to choose a suitable propagation mode for the SAW device especially when it is designed for microfluidic applications: Rayleigh SAW mode is the best suited for space-charge related applications as most of the energy in this mode is concentrated within one wavelength of the substrate".
As the aspect ratio of the electrode finger length to the spatial wavelength increases, the numerical simulation and theoretical modeling is simplified by not considering the third dimension (depth), and so also the electro-mechanical coupling along this direction. In this way, the 3D model is reduced to a 2D one. As Ramishev and Rajan[5] report that, for this reason, sophisticated models of electrical or acoustical couplings are often developed using 2D approximations.
As this consideration is made, all the simulations in this section are carried out taking into account only two dimensions.
Numerical simulations have been carried out by using COMSOL$^{\text{TM}}$ 5.5, and taking advantage of three interfaces:

- *Solid mechanics* interface, in order to describe the mechanical properties of the substrates;
- *Electrostatics* interface, to model the electrical behavior of the devices;
- *Piezoelectric Effect* Multiphysics, aimed to implement the coupling between the two previous interfaces.

In this chapter, no fluid is supposed to cover the piezoelectric layer: all the simulations assume the upper surface to be free, in order not to consider any attenuation of the resulting displacement or resonant frequency variation.
In order to isolate different aspects regarding surface acoustic waves, the first approach was to simulate the phenomenon starting from a simple model and moving to a more realistic one as new details are introduced.
For this reason, first it has been simulated just **one single pair of electrodes** and a *periodic boundary condition* has been applied at the sides, as displayed in fig. 3.1.
Subsequently, a model including a **finite number of pairs** is considered,

and no periodic boundary conditions are applied: this approach allows to better study the behaviour of SAW, as it is shown in the following sections. Table 3.1 shows the involved parameters for the simulations regarding the study of SAW, while table 3.2 reports the materials that have been used to carry out such simulations.

| **Parameter** | **Symbol** | **Unit** | **Value** |
|---|---|---|---|
| Width of the electrodes | $w_{el}$ | m | $\frac{\lambda}{4}$ |
| Height of the electrodes | $h_{el}$ | m | $1{\cdot}10^{-7}$ |
| Operating frequency | $f_0$ | Hz | $\frac{2\pi}{\lambda}$ |
| Width of the piezoelectric substrate | $w_{piezo}$ | m | $7{\cdot}10^{-4}$ |
| Height of the piezoelectric substrate | $h_{piezo}$ | m | $3{\cdot}10^{-6}$ |
| Applied voltage | $V_0$ | V | (not fixed) |

Table 3.1: Parameters involved in FEA simulations for surface acoustic waves. $\lambda$ is the wavelength of the IDT pattern.

| **Part** | **Material** |
|---|---|
| Electrodes | Aluminum |
| Substrate | Silicon |
| Piezoelectric layer | PZT-5H |

Table 3.2: Materials involved in in FEA simulations for surface acoustic waves

## 3.1 Single-pair approach

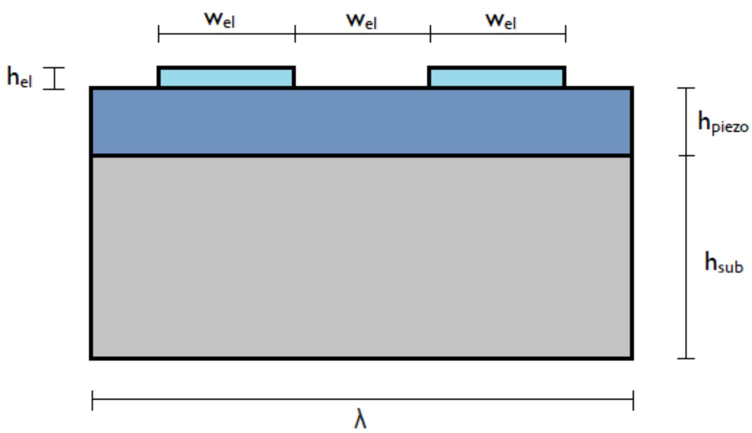


Figure 3.1: Conceptual drawing for a simulation with a single pair of electrodes: the grey region represents the Silicon substrate, the blue one the piezoelectric layer, and the light blue one the electrodes.

First it is analyzed how the height of the piezoelectric layer affect the location of the resonant peak in the frequency response of the device. As it can be predicted, fig. 3.2 shows that the resonant frequency approaches to a specific value (1.99MHz) as the height of the piezoelectric layers increases. The convergence is attributable to lower and lower contribution of the reflections from the bottom side. Indeed, as proved by eq. 2.21, acoustic ways are attenuated as they approach to the bottom side of the piezoelectric substrate, and so the reflected back waves are supposed to be doubly attenuated at the free surface.
Fig. 3.3 shows that the same trend is obtained if a different working frequency (different $\lambda$) is chosen.

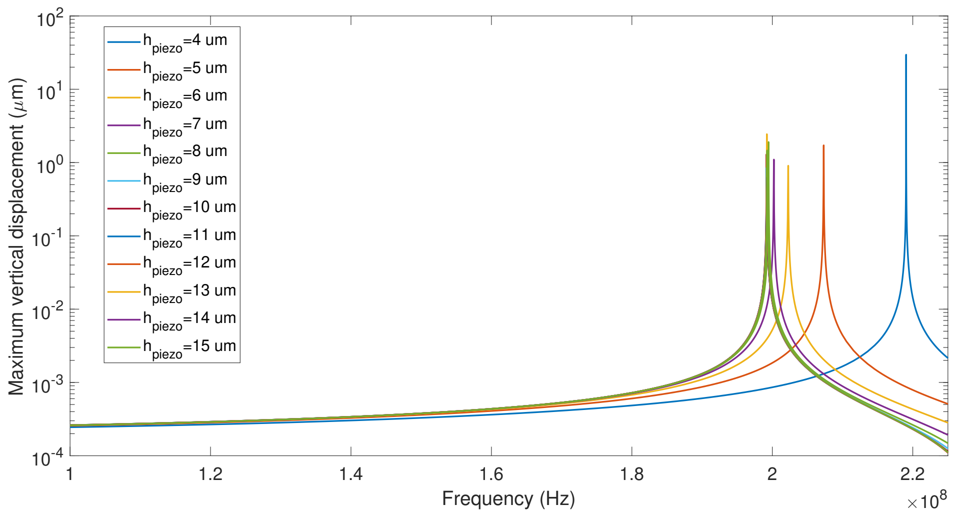


Figure 3.2: Frequency response with $\lambda = 10\mu m$, $h_{sub} = 70\mu m$, $V_0 = 1V$

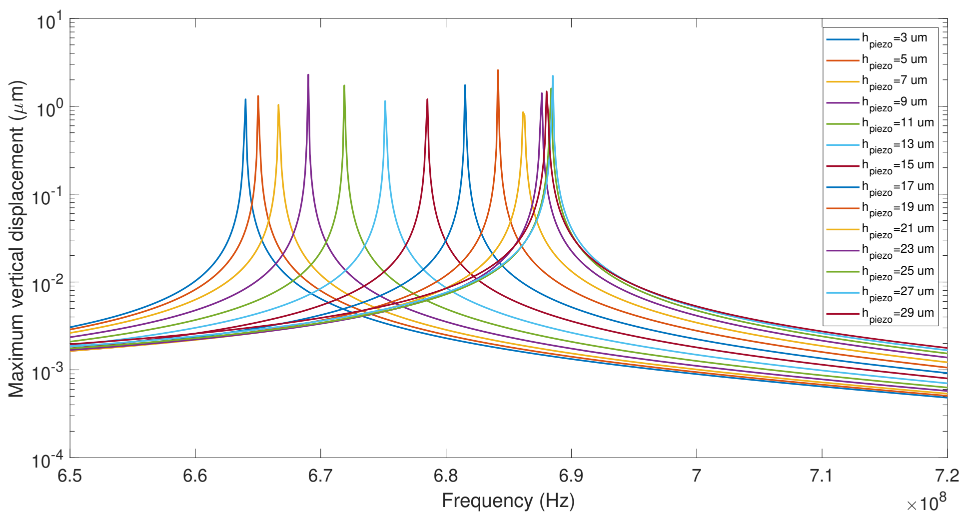


Figure 3.3: Frequency response with $\lambda = 3\mu m$, $h_{sub} = 70\mu m$, $V_0 = 1V$

Finally it is investigated how the role of the height of the Silicon substrate influences the location of the resonant peak. From fig. 3.4, no variations is relevant: the reason is explainable by considering that the height of the piezoelectric layers is sufficient to avoid reflections, and so the height of the Silicon substrate does not result to be important.

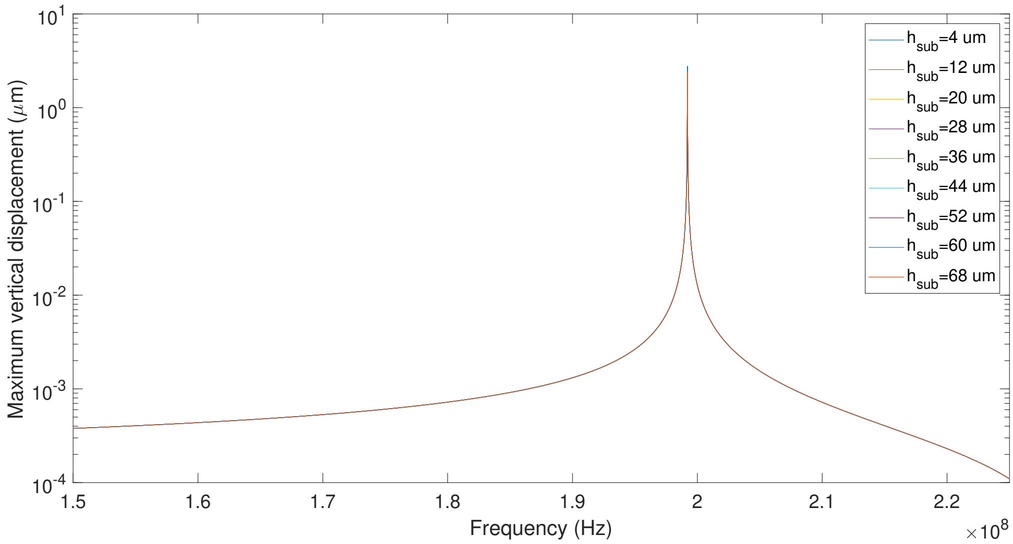


Figure 3.4: Frequency response with $\lambda = 10\mu m$, $h_{piezo} = 12\mu m$

## 3.2 Multiple-pair approach

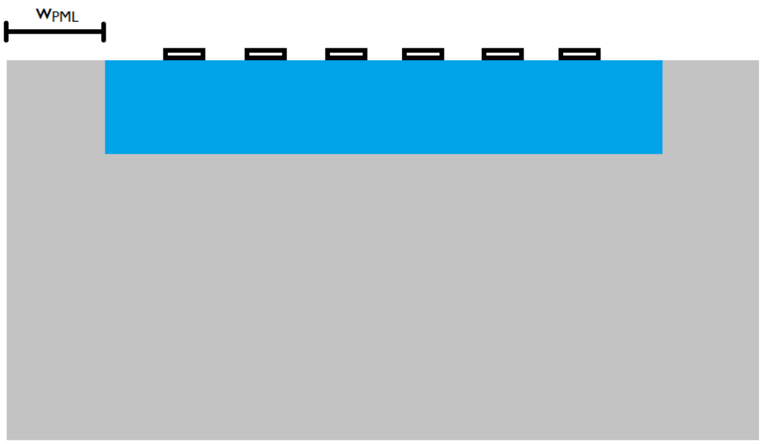


Figure 3.5: Concept of surface acoustic waves: the grey region represents the PML, the blue one the piezoelectric layer.

In the real world, periodic boundary conditions do not exist. For this reason, the *single-pair model* is not sufficient to fully comprehend the behaviour of

SAW travelling on a piezoelectric layer.
Moreover, the previous simulations do not take into account the *damping* effect, which are due to the inner physical properties of the materials of the device. A more sophisticated model is presented in the following sections, but first it is necessary to introduce two distincts concepts: the **perfectly matched layer** and the **material dampings**.

### Perfectly matched layer (PML)

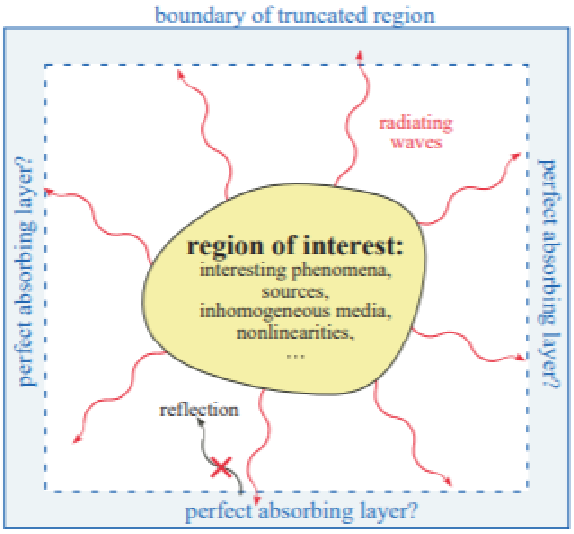


Figure 3.6: Concept scheme of PML[44]

As shown in the previous section, the geometrical features of the piezoelectric layer and the Silicon substrate play a crucial role in this analysis, since they affect both the SAW amplitude, and the location of the resonant peak. In this section it has been decided to neglect their contribution introducing the definition of a *perfectly matched layer* (PML): the purpose is avoiding the reflection of surface acoustic waves at the left and right boundaries and from the bottom of the structure.
An acoustic wave is attenuated exponentially as it travels through an absorbing layer. At the same time, whenever it transits from one material to another, two reflection phenomena occur:

- three waves reflect when propagating from the a non-absorbing to the absorbing layer[44];
- three waves reflect when passing from absorbing to non-absorbing material[44].

The possibility of extending the concept of PML proposed by Berenger[45] for electromagnetic waves to the elastodynamic case is discussed by Chew and Liu[46].

COMSOL provides the possibility of defining a PML, and the simulations in this section have been carried out by setting a surrounding boundary layer to avoid reflections from the bottom and lateral parts of the substrate (fig. 3.5).

**Damping in piezoelectric materials**

Losses in piezoelectric materials are generally devided into three groups[47]:

- **mechanical** losses (caused by a combination of power absorption and and scattering), introduced by adding an imaginary component to the terms of the stiffness and compliance matrices

$$\tilde{c}_E^{m,n} = c_E^{m,n}(1 + i\eta_{cE}^{m,n}) \tag{3.1}$$

$$\tilde{s}_E^{m,n} = s_E^{m,n}(1 - i\eta_{sE}^{m,n}) \tag{3.2}$$

- **dielectric** losses (attributed to bound charge and dipole relaxation phenomena), represented by adding an imaginary component to the terms of the permittivity matrices

$$\tilde{\epsilon}_{rS}^{m,n} = \epsilon_{rS}^{m,n}(1 - i\eta_{\epsilon S}^{m,n}) \tag{3.3}$$

$$\tilde{\epsilon}_{rT}^{m,n} = \epsilon_{rT}^{m,n}(1 - i\eta_{\epsilon T}^{m,n}). \tag{3.4}$$

- **coupling** losses, represented by adding an imaginary component to the terms of the coupling matrices.

$$\tilde{d}^{m,n} = d^{m,n}(1 + i\eta_d^{m,n}) \tag{3.5}$$

$$\tilde{e}^{m,n} = e^{m,n}(1 + i\eta_e^{m,n}) \tag{3.6}$$

As regards the following simulations in this chapter, an isotropic loss factor $\eta_{cE} = 84.6339 \cdot 10^{-3}$[48] is included.

### 3.2.1 Results

In this subsection, the optimal width of the PML at the sides of the substrate is chosen by carrying out proper simulations: they result to be fundamental to investigate how piezoelectric nonlinearities and the number of IDT pairsi influence the final performances of the device. First it is investigated the influence of $\mathrm{w}_{PML}$ on the maximum vertical displacement of the piezoelectric substrate.
At this purpose there are carried out three simulations characterized by a different height of the piezoelectric substrate, while keeping fixed the height of the Silicon substrate ($70\mu m$), the applied voltage (1V) and using a single IDT pair.
As shown in fig. 3.7, 3.8 and 3.9, the value of $\mathrm{w}_{PML}$ does not affect dramatically the resulting maximum displacement for any of the chosen values for $h_{piezo}$: indeed the relative variation between the minimum value and the

maximum one is 0.09%, 0.11% and 0.03% respectively.
This verifications of course do not have any physical value, but are worth at the aim of getting a simulation as close as possible to the reality.

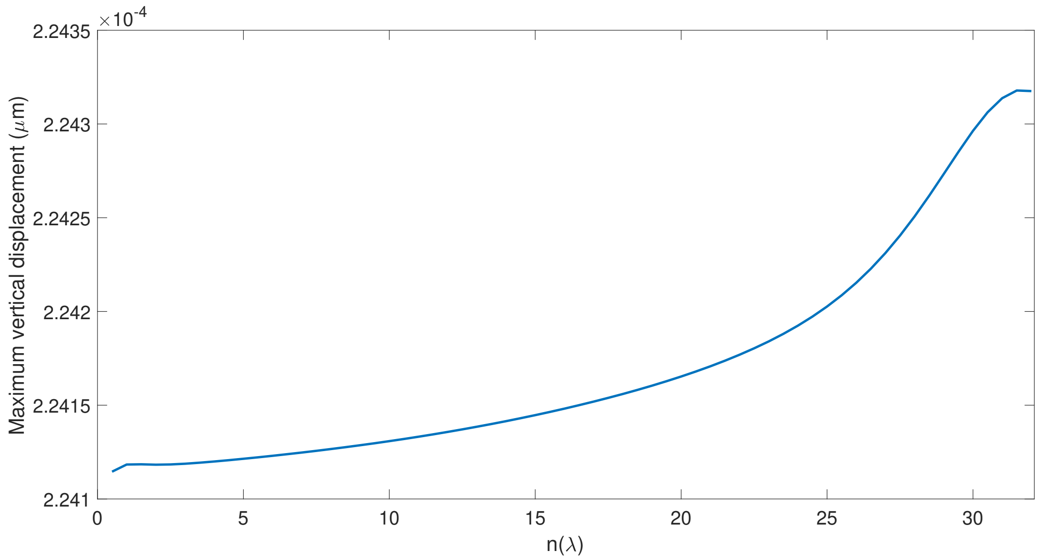


Figure 3.7: Maximum vertical displacement of the free surface by varying the length of the lateral PML layers (normalized by $\lambda$), when $h_{piezo} = 12\mu m$

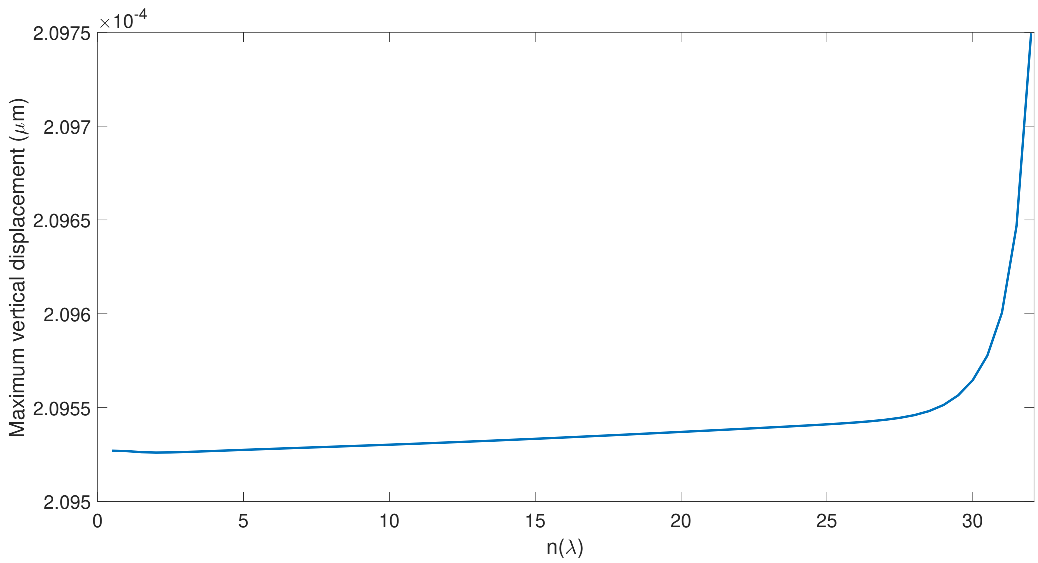


Figure 3.8: Maximum vertical displacement of the free surface by varying the length of the lateral PML layers (normalized by $\lambda$), when $h_{piezo} = 3\mu m$

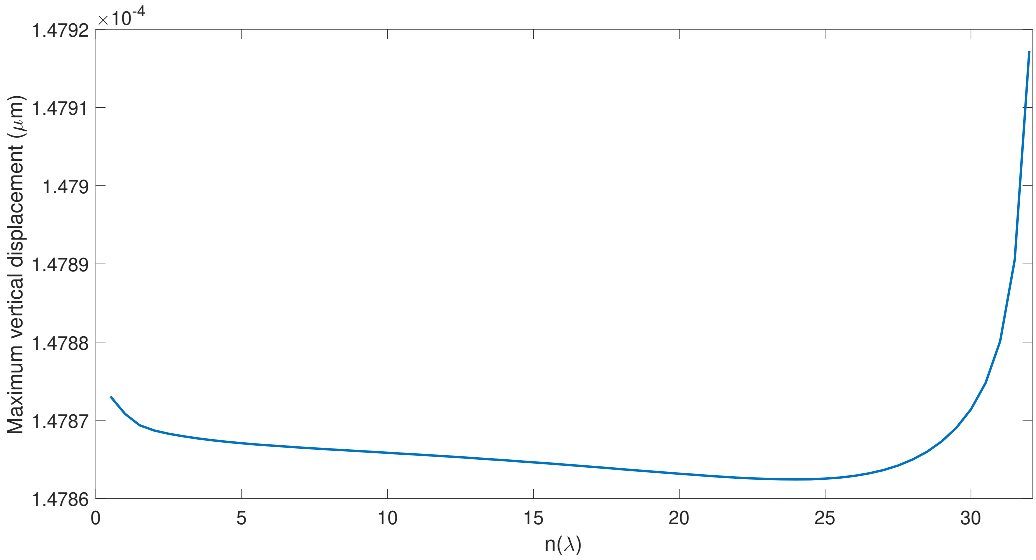


Figure 3.9: Maximum vertical displacement of the free surface by varying the length of the lateral PML layers (normalized by $\lambda$), when $h_{piezo} = 1\mu m$

Secondly, it is discussed about the optimal number of IDTs in order to get the heighest displacement has possible. At this aim, it has been decided to fix w$_{PML}$ ($3\lambda$), the height of the piezoelectric layer ($3\mu m$) and the height of the Silicon substrate ($70\mu m$) and V$_0$ (1V): fig. 3.10 and 3.11 clarify that 25 pairs are sufficient to reach the convergence of the maximum displacement independently from the operating frequency.

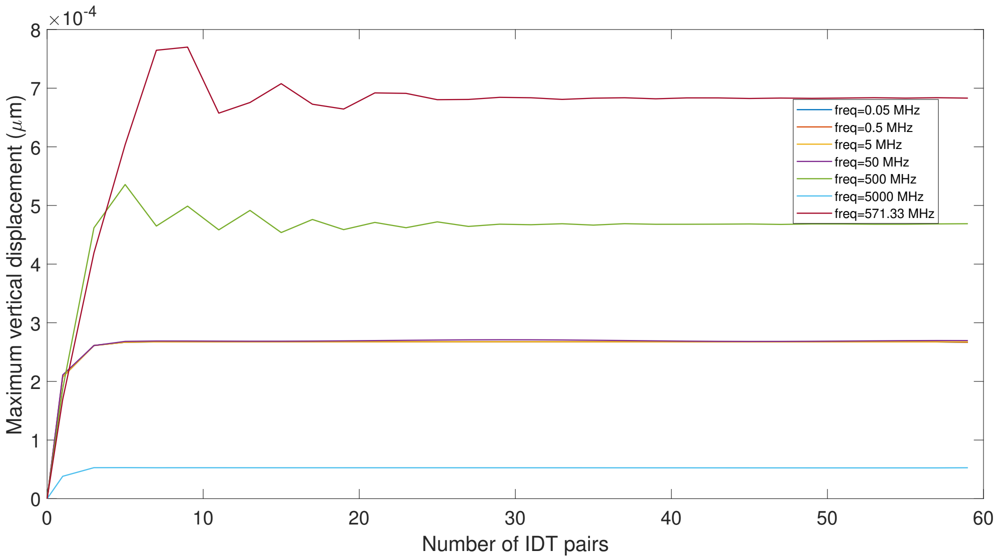


Figure 3.10: Maximum vertical displacement at the free surface by varying the number of IDT pairs

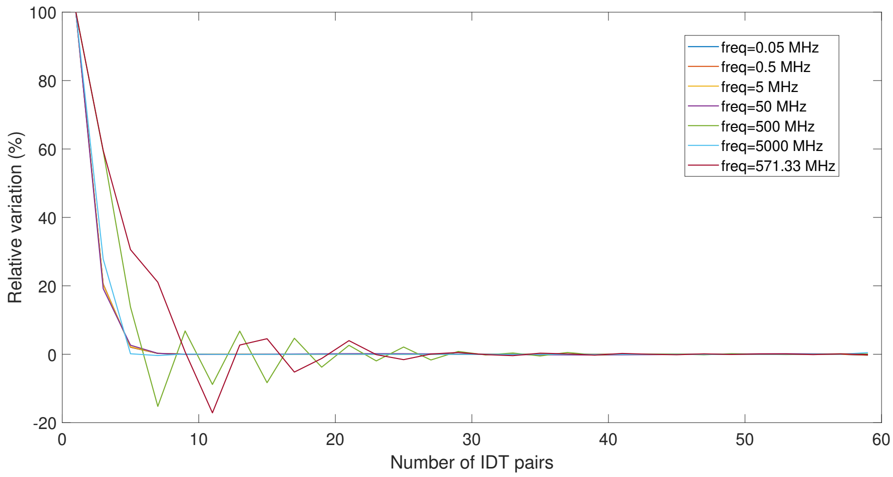


Figure 3.11: Relative variation of the maximum vertical displacement at the free surface by varying the number of IDT pairs

Subsequently the role of geometrical non-linearities over the maximum reachable displacement is investigated.
As operated for the previous analysis, it has been decided to fix w$_{PML}$ ($3\lambda$), the height of the piezoelectric layer ($3\mu m$) and the height of the Silicon substrate ($70\mu m$), the number of IDT pairs (35) and the operating frequency (571.33MHz): fig. 3.12 and 3.13 prove that it is convenient to work in a range 0-400V, when the relative difference between the linearized and the non-linearized behaviours is 19.36%. However, it is very unlikely to reach such high voltages in real life applications.

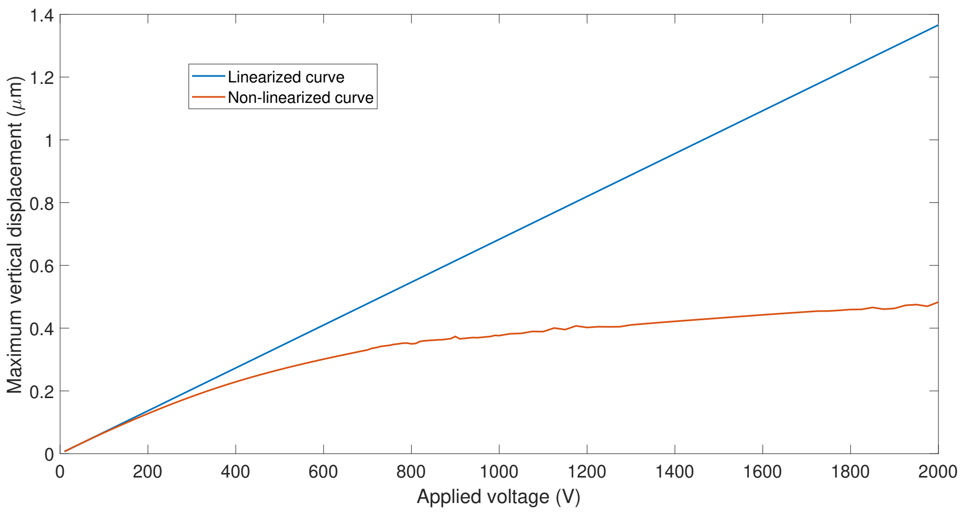


Figure 3.12: Electro-mechanical behavior of the piezoelectric substrate when geometrical non-linearities are considered (blue curve) and when they are not (red curve)

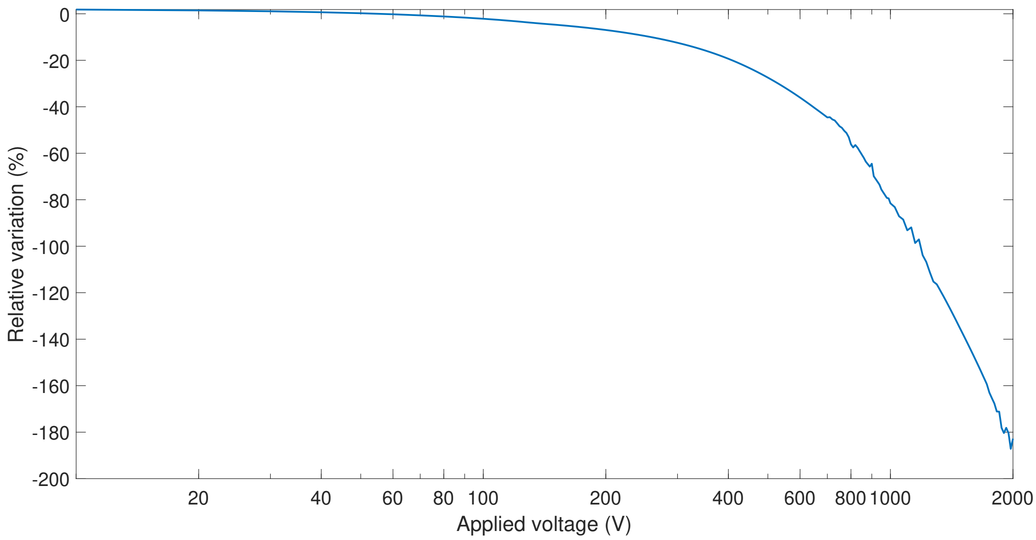


Figure 3.13: Relative discrepancy between the linear and the non-linear electro-mechanical characteristics of the piezoelectric layer

Finally, the frequency response of the device is simulated when fixing $\lambda$ ($3\mu m$): it is observe if the position of the first resonant peak corresponds is located where expected ($f = \frac{c_{SAW}}{\lambda}$, with $c_{SAW}$ being the wave speed of the piezoelectric layer and $\lambda$ the wavelength of the device), as previously explained in section 1.1.
Fig. 3.14 shows how a discrepancy of 12.39% is present with respect to the theoretical resonant frequency: this discrepancy suggests that the formula fairly predicts the position of the peak, but it is expected that more details should be included to get a more precise prediction.

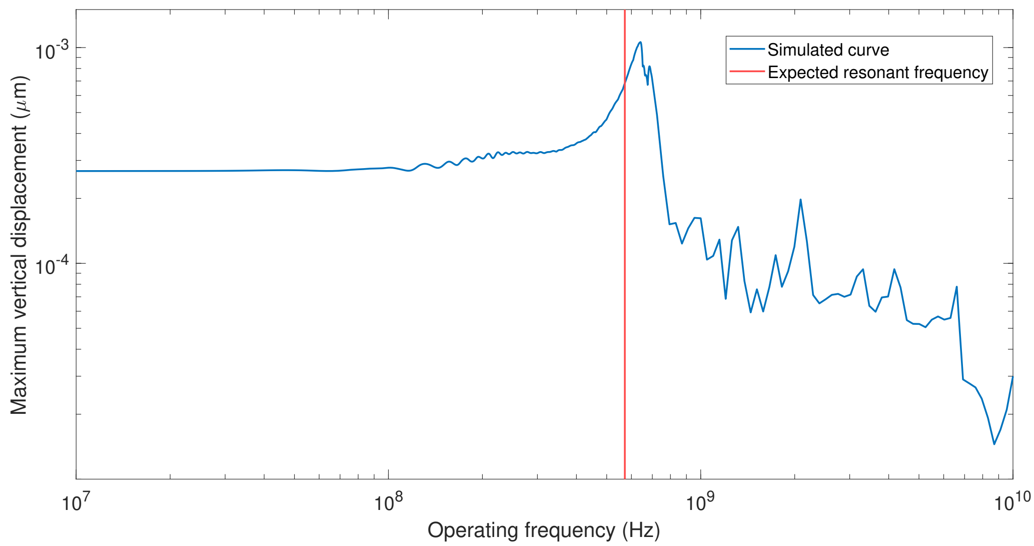


Figure 3.14: Frequency response of PZT-5H in the range 10MHz-10GHz

The results discussed in this section are aimed to understand the requirements to maximize the amplitude of SAW when a certain sinusoidal signal is applied.
However, the piezoelectric coupling is not involved in the simulations of next chapter: the applied voltage affect the microfluidic flow through the generated acoustic waves, so the electro-mechanical coupling is not directly involved in the acoustic streaming.
So, a proper boundary condition is applied to avoid electrodes and the piezoelectric layer to be included, so that the computational time is reduced.

# Chapter 4

# Numerical simulations of acoustofluidics

In this chapter it is shown how to model different acoustofluidic case studies by applying proper boundary conditions.
In this section it is investigated the numerical modelling of the acousto-fluidic interface: at this purpose it has been fundamental the contribution of the previous literature [42][49], since the implementation of the necessary fluidic boundary conditions is not straightforward.
High focus is dedicated to 2D numerical simulations: since a deep a study on the optimal operating frequency as to be achieved, it is decided to neglect the depth of the channel to reduce as much as necessary the size of the finite elements.
At the end of the chapter, results of 3D simulations are reported to compare the performances of an acousto-fluidic pump with its electro-osmotic counterpart.
As the case of the numerical simulations in the previous chapter, models are implemented by COMSOL$^{TM}$ 5.5.
All the FEA simulations in this chapter are carried out by implement two distinct interfaces:

- *Thermoviscous Acoustics - Frequency Domain*, which allows to introduce the acoustic boundary conditions. It is associated to a *Frequency Domain* study, that is aimed to compute the acoustic fields by solving $1^{st}$-order equation 2.43;

- *Laminar flow*, which introduces the fludic boundary condition. It is associated to a *Stationary* study, which is carried out after the Frequency Domain one. The reason relies on the fact that no *Acoustofluidic* Multiphysics interface is available, so the Stationary study requires to postprocess the results of the previous simulation to solve eq. 2.54.

Table 4.1 reports the geometrical parameters of channel that are fixed throughout all the simulation.
Table 4.2 shows the names of the variables involved in acoustofluidic simulations. As previously highlighted, two terms require to be computed to

| Physical entity | Symbol | Expression | Unit of measurement |
|---|---|---|---|
| Height | $H$ | $10^{-4}$ | $m$ |
| Width | $W$ | $10^{-4}$ | $m$ |
| Length | $L$ | $10^{-3}$ | $m$ |

Table 4.1: Geometrical parameters of channel for acoustofluidic simulations

| Variable | Symbol | Unit of measurement |
|---|---|---|
| Acoustic velocity along x-direction | u1 | $m \cdot s^{-1}$ |
| Acoustic velocity along y-direction | v1 | $m \cdot s^{-1}$ |
| Acoustic velocity along z-direction | w1 | $m \cdot s^{-1}$ |
| Acoustic pressure | p1 | $Pa$ |
| Streaming velocity along x-direction | u2 | $m \cdot s^{-1}$ |
| Streaming velocity along y-direction | v2 | $m \cdot s^{-1}$ |
| Streaming velocity along z-direction | w2 | $m \cdot s^{-1}$ |
| Streaming pressure | p2 | $Pa$ |

Table 4.2: Variables involved in acoustofluidic simulations

fully couple the acoustic domain with the microfluidic one: **volume force** and **mass-source** terms.
Since the way they are included is not considered to be straightforward, in the following the script used for FEA simulations is reported:

- **volume force term**, introduced through the *Laminar flow* interface, has three components along $x$, $y$ an $z$ directions. They correspond respectively to eq. 4.1, 4.2 and 4.3, and are reported how should be implemented on COMSOL.

$$\begin{aligned} F_x &= -0.5\text{*real[ta.iomega*conj(ta.rho)*u1]-ta.rho0*0.5*(real(conj(u1)*d(u1,x))} \\ &\qquad + \text{real(conj(v1)*d(u1,y))} + \text{real(conj(w1)*d(u1,z)))} \end{aligned} \tag{4.1}$$

$$\begin{aligned} F_y &= -0.5\text{*real[ta.iomega*conj(ta.rho)*v1]-ta.rho0*0.5*(real(conj(u1)*d(v1,x))} \\ &\qquad + \text{real[conj(v1)*d(v1,y)]} + \text{real(conj(w1)*d(v1,z)))} \end{aligned} \tag{4.2}$$

$$\begin{aligned} F_z &= -0.5\text{*real[ta.iomega*conj(ta.rho)*w1]-ta.rho0*0.5*(real(conj(u1)*d(w1,x))} \\ &\qquad + \text{real[conj(v1)*d(w1,y)]} + \text{real(conj(w1)*d(w1,z)))} \end{aligned} \tag{4.3}$$

- **mass-source term**, included as a *Weak contribution* through *Weak form PDE* interface. Eq. 4.4 shows how it is implemented.

$$\begin{aligned} &\text{[-d(0.5*real(conj(ta.rho)*u1),x)-d(0.5*real(conj(ta.rho)*v1),y)} \\ &\qquad \text{-d(0.5*real(conj(ta.rho)*w1),z)]*test(p2)} \end{aligned} \tag{4.4}$$

where test(p2) is a *test function*, whose nature is not discussed in this document. It is sufficient to remember that its presence is linked to the *weak formulation* of differential equations, allowing to involve also non-smooth functions with respect to *partial differential equations* (PDE), and so also less strict.

## 4.1 2D numerical simulations

Two study cases are analyzed to determine the optimal working frequency to reach the higher flow rate at the outlet - in case of channels with two open ends - or the maximum average internal velocity in case a totally close tube is considered.
In this section all the simulations are carried out neglecting the variations along z-component: computational time is reduced without renouncing to the size of finite elements to be as small as necessary.
In both the cases, it supposed the SAW to be exited from the left of the channel, as displayed in fig. 4.1.

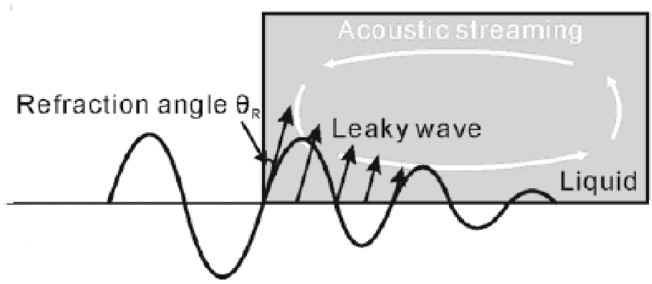


Figure 4.1: Conceptual drawing highlighting the source of the SAW[50]

### 4.1.1 Rectangular tube with two open ends

In fig. 4.2 it is pictured the device analysed in this section.

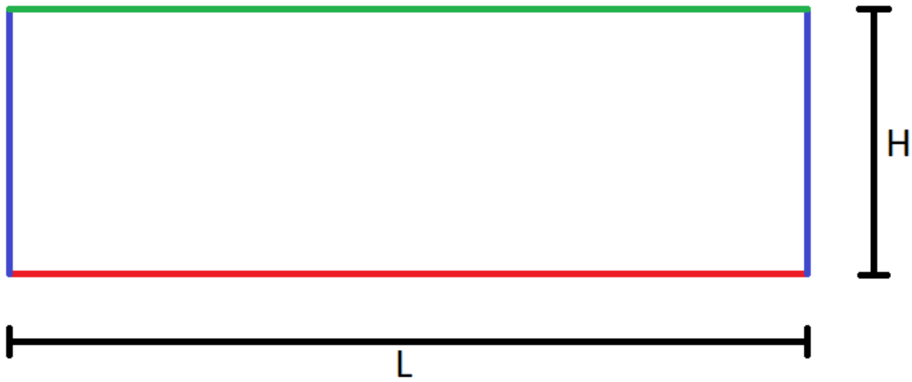


Figure 4.2: Drawing of the tube analyzed in this section. The green line indicates the presence of a *wall* boundary condition, the red line refers to the propagation of *surface acoustic waves*, and blue one the *inlet* (left side) and the *outlet* (right side) of the channel.

### Boundary conditions

The following boundary conditions are applied for this study case:

- **acoustic velocity**[51] along the bottom side of the channel

$$\begin{cases} u_{1x} & = \text{1.2*u0*ta.iomega*cos(k*x)*exp(-alpha*x)} \\ u_{1y} & = \text{-2*u0*ta.iomega*cos(k*x)*exp(-alpha*x)} \end{cases} \tag{4.5}$$

  where $u_0$ is the maximum displacement at the bottom side, $k$ is equal to $\frac{2\pi f}{c_{SAW}}$, and *alpha* is the attenuation coefficient given by eq. 2.24. If a interval of operating frequences is considered to be 1-10MHz and $L = 1\text{mm}$, the maximum attenuation ranges 6-47% at the end of the channel. For this reason, the attenuation coefficient is not expected to affect particularly the results;

- **acoustic pressure** at the inlet and outlet

$$p_1 = 0\text{Pa} \tag{4.6}$$

- **streaming pressure** at the inlet

$$p_2 = 0\text{Pa} \tag{4.7}$$

### Results

First it is investigated how the size of the finite elements affects the average velocity at the outlet of the channel.
At this purpose, it is fixed the maximum size of the elements to $\lambda/4$ and the minimum one to $\lambda/8$, and imposed a *Distribution* boundary condition for the mesh. In particular, named $n_{el}$ the number of elements along the

lateral edges of the channel, the number of elements along the top and bottom edges is fixed to $10n_{el}$.
Fig. 4.3 and 4.4 prove that at 1MHz $n_{el}$ is required to be at least 10, in order to guarantee the precision of the simulations.
Fig. 4.5 and 4.6 prove that at 10MHz $n_{el}$ is required to be at least 250 in order to guarantee an error under ±5%. At this purpose, since the results presented in the following are carried out in the range of frequencies up to 10MHz, it has been decided to fix $n_{el}$ to 250.
Subsequently it is analysed how the operating frequency influences the average velocity detected at the outlet of the channel: fig. 4.7 clearly shows that the resonant peaks of the average horizontal velocity are located following the law

$$f_{res} = n \cdot \frac{c_f}{2L} \tag{4.8}$$

where $n$ is a natural number, $L$ the length of the channel, and $c_f$ is the speed of sound for a specific fluid.

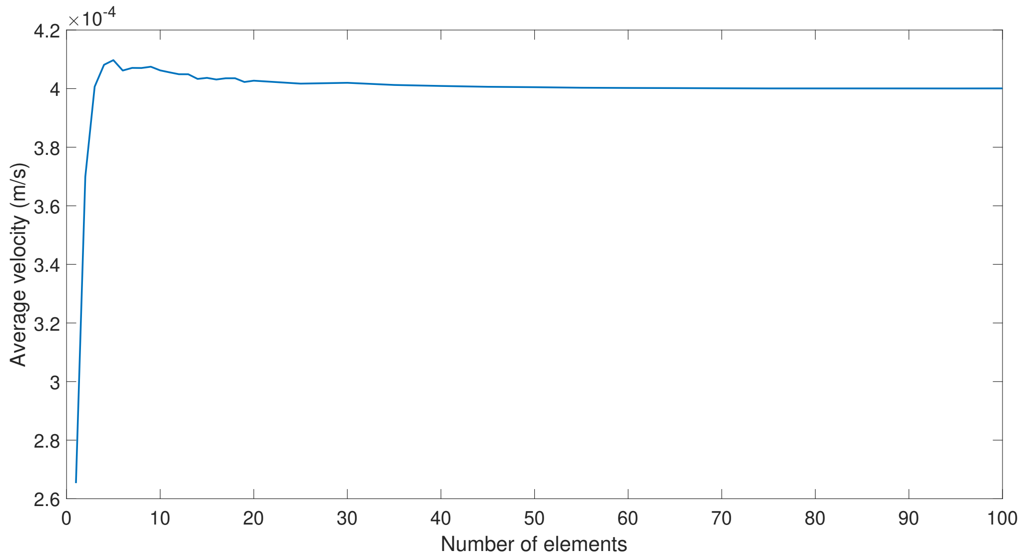


Figure 4.3: Influence of the number of elements ($n_{el}$) over the average flow velocity at the outlet when the acoustic wave frequency is 1MHz and $u_0$ 1nm

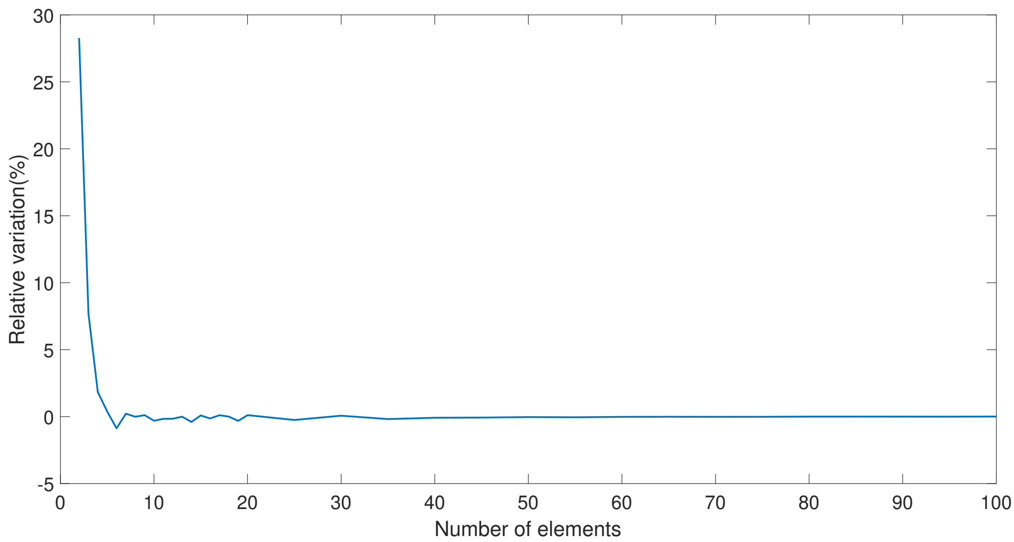


Figure 4.4: Influence of the number of elements ($n_{el}$) over the relative variation of average flow velocity at the outlet when the acoustic wave frequency is 1MHz and $u_0$ 1nm

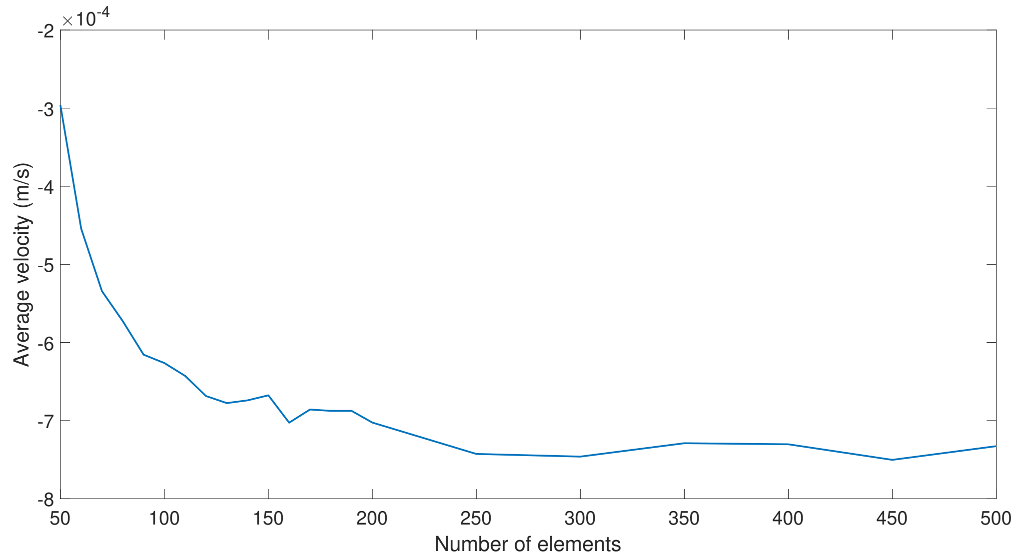


Figure 4.5: Influence of the number of elements ($n_{el}$) over the average flow velocity at the outlet when the acoustic wave frequency is 10MHz and $u_0$ 1nm

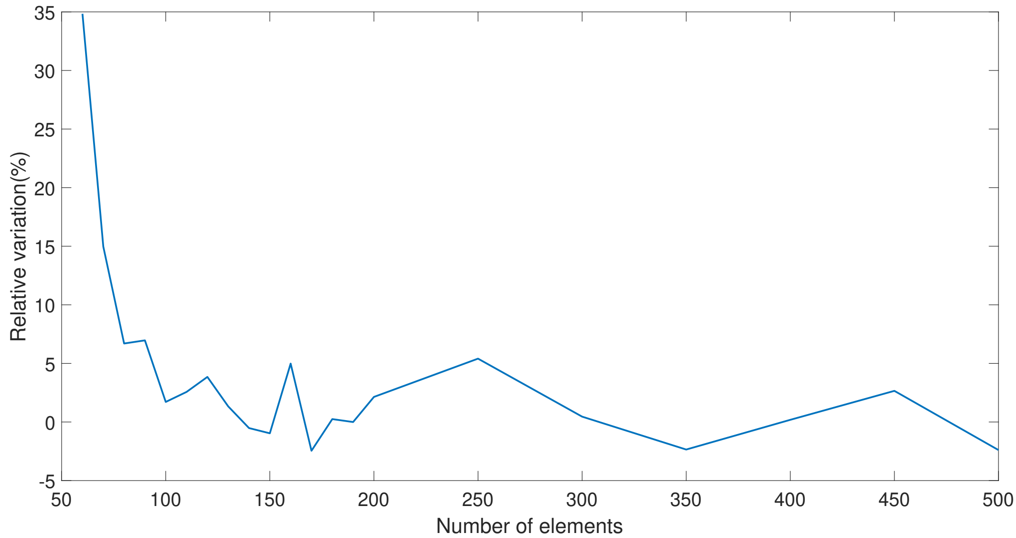


Figure 4.6: Influence of the number of elements ($n_{el}$) over the relative variation of average flow velocity at the outlet when the acoustic wave frequency is 10MHz and $u_0$ 1nm

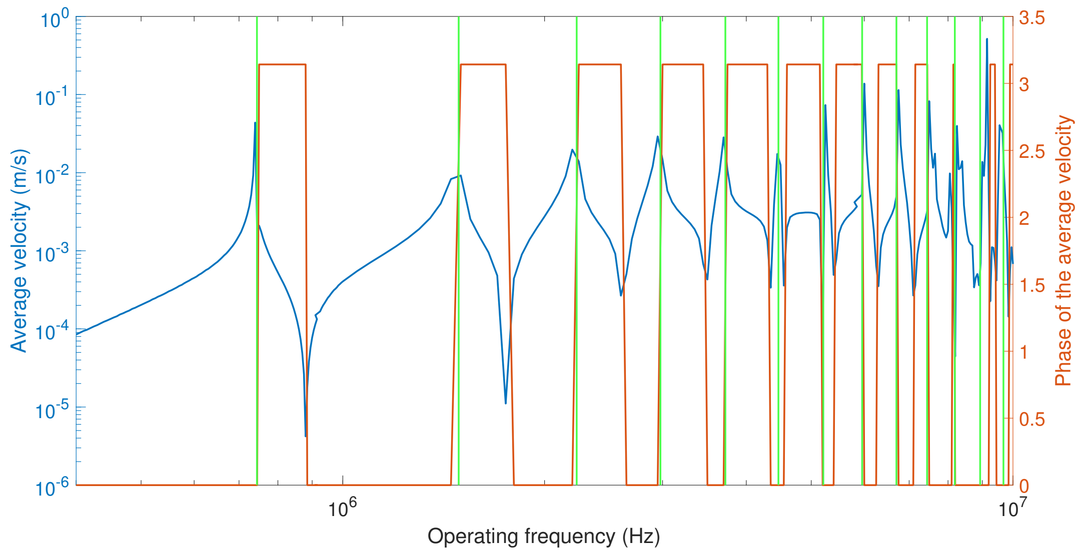


Figure 4.7: Frequency response for a rectangular channel with two open ends, with $u_0$ to to 1nm. The *blue* curve shows the absolute value of the average horizontal velocity, the *red* one its phase and the *green* vertical lines the expected resonant peaks (see eq. 4.8).

It is investigated how $u_0$ (i.e. the maximum SAW displacement) influences the average speed at the outlet: for the following simulations it has been decided to fix the operating frequency at $f_{res}$ with $n = 1$.
As executed previously, first it is fundamental to choose a proper value for $n_{el}$: at this purpose it has been decided to carry out the simulations posing $u_0$ to 10nm, since it represents the maximum simulated value (as can be

seen from fig. 4.10) and so represents the most critical case. Fig. 4.8 and 4.9 prove that $n_{el}$ can be fixed to 100 in order to obtain accurate results.
Fig. 4.10 shows the correlation between $u_0$ and the average velocity at the outlet: through *Curve Fitting* (extension by MATLAB$^{TM}$) it is proved that this curve fits a quadratic curve in the form

$$v_{av} = a \cdot u_0^2 \tag{4.9}$$

where $v_{av}$ is the average velocity at the outlet, $a$ is set to $9.44{\cdot}10^{15}$ to get an R-square factor of 0.9864.
The origin of the value of the fitting parameter $a$ is not studied, but it is interesting to notice the same trend as highlighted by Rayleigh[16] with different boundary conditions.

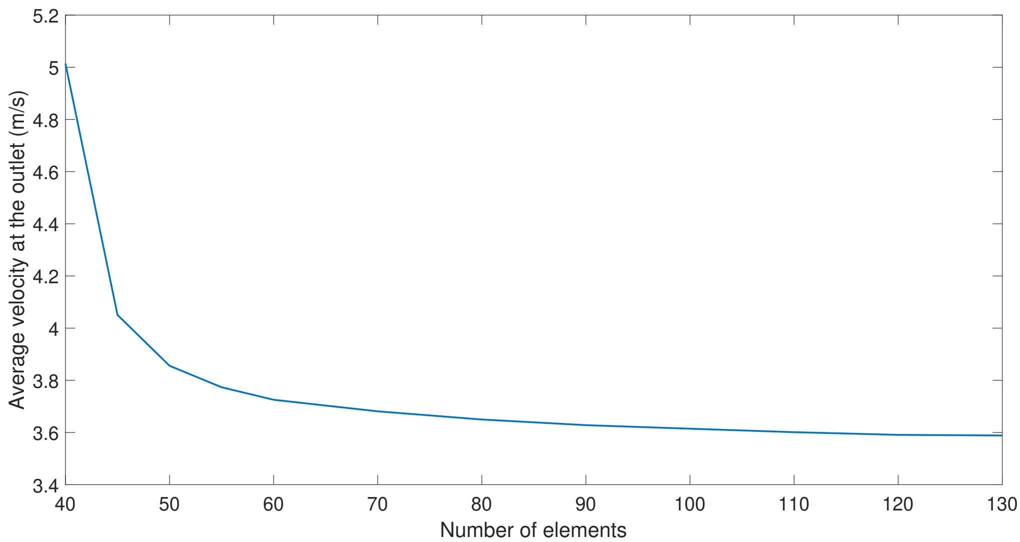


Figure 4.8: Influence of $n_{el}$ over the average velocity at the outlet of the channel

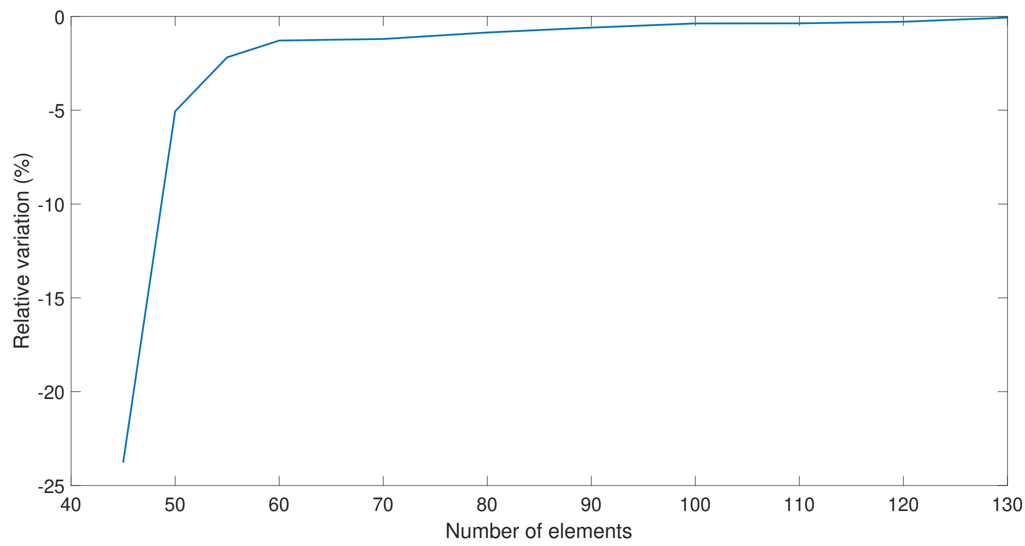


Figure 4.9: Influence of $n_{el}$ over the relative variation of the average velocity at the outlet of the channel

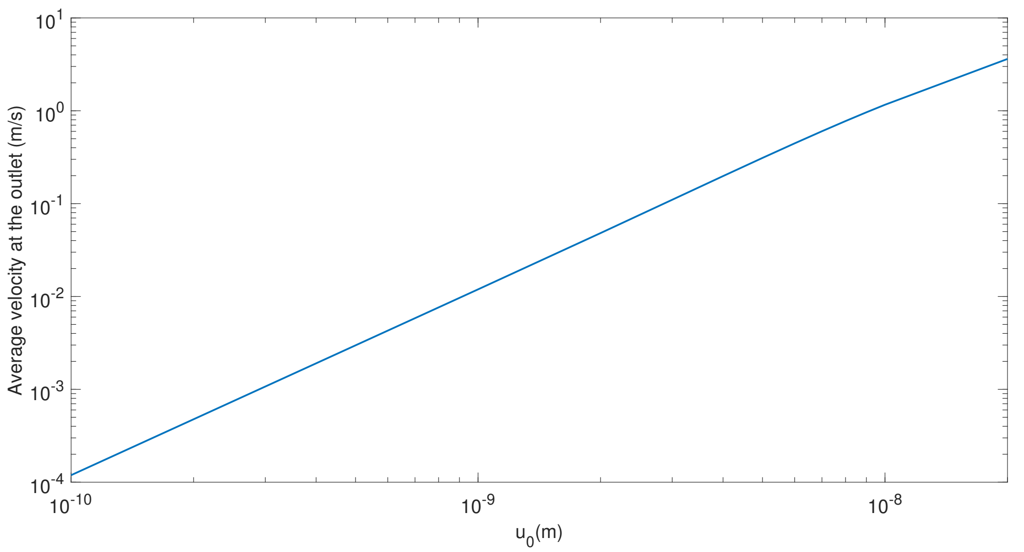


Figure 4.10: The graph shows the relation between $u_0$ and the average velocity at the outlet of the channel when the channel has an inlet and an outlet

### 4.1.2 Rectangular tube with two closed ends

In fig. 4.11 it is pictured the device analysed in this section.


Figure 4.11: Drawing of the tube analyzed in this section. Green lines indicate the presence of a *wall* boundary condition, while the red line refers to the propagation of *surface acoust waves*.

### Boundary conditions

The following boundary conditions are applied for this study case:

- **acoustic velocity** along the bottom side of the channel

$$\begin{cases} u_{1x} & = & \text{1.2*u0*ta.iomega*cos(k*x)*exp(-alpha*x)} \\ u_{1y} & = & \text{-2*u0*ta.iomega*cos(k*x)*exp(-alpha*x)} \end{cases} \tag{4.10}$$

- **pointwise weak contribution**[52]

$$\text{aveop1(p2)*test(Im)} \tag{4.11}$$

  where $Im$ is an auxiliary dependant variable and *aveop1* is a $4^{th}$-order average operation.

- **domain weak contribution**[52]

$$\text{intop1(Im)*test(p2)} \tag{4.12}$$

  where *intop1* is a $4^{th}$-order integration operation.

### Results

The results obtained about the mesh, presented in section 4.1.1, are applied for this case study: $n_{el}$ is fixed to 250.
As previously done, also in this case it is investigated how the operating frequency influences the average velocity detected at the outlet of the channel: fig. 4.12 proves that the resonant peaks of the average horizontal velocity follow the same law as the case of a rectangular tube (eq. 4.8).
Fig. 4.14 (blue curve) shows the correlation between $u_0$ and the average velocity at the outlet: as done for the previous case study, it is proved that it fits eq. 4.9, where $a$ is set to $4.379 \cdot 10^{14} m^{-1} s^{-1}$ to get an R-square factor equal to 1.

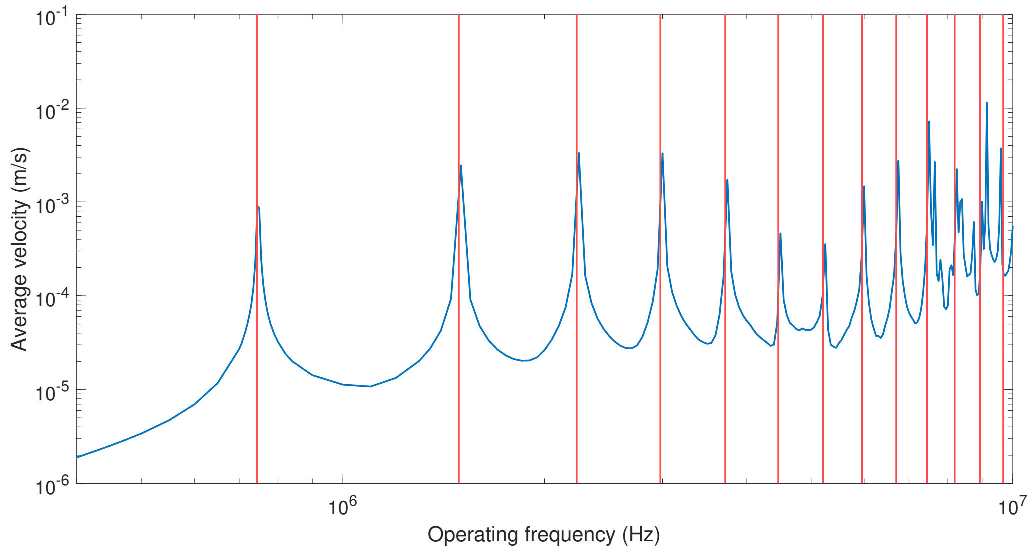


Figure 4.12: Frequency response for a rectangular channel with two open ends. The *blue* curve shows the absolute value of the average horizontal velocity and the *red* vertical lines the expected resonant peaks (see eq. 4.8).

In the following it is analyzed how the presence of **PDMS walls** could influence the average internal velocity. Unfortunately, because of geometrical complexities which are almost unavoidable in SAW acoustofluidics, analytical solutions are difficult to achieve: this is the reason why it is natural for researchers to resort to mathematical simulations[51].
Three ways of modeling PDMS are possible for acoustic simulations[53]:

- PDMS is described as linear elastic solid material through the *Solid Mechanics Interface*. This approach resembles on the full model of the phenomenon and includes the propagation of shear waves in PDMS (unless a low-reflecting boundary condition is set at the top of the tube);

- PDMS is treated as a *non-flowing fluid* through the *Pressure Acoustic Interface*, so the contribution of shear waves is not included, while wave leakage at the substrate–PDMS interface is;

- PDMS contribution is mathematically modeled as a normal impedance

$$Z_0 = \rho_m c_m \tag{4.13}$$

  where $\rho_m$ is the density of PDMS (1070 kg/m$^3$) and $c_m$ the associated longitudinal wave speed (1030 m/s).

Since it has been proven the three approaches to be consistent with each other[53], the third path is chosen to minimize the computational effort. Fig. 4.13 reveals that the resonant peaks - observed in fig. 4.12 - disappear when PDMS impedance is included, and a sensitive variation of the modulus occurs. It is particularly evident in fig. 4.14, where the red curve follows eq. 4.9 if $a$ is set to $1.61{\cdot}10^{12} m^{-1} s^{-1}$: the trend is the same, but the fitting coefficient is attenuated.

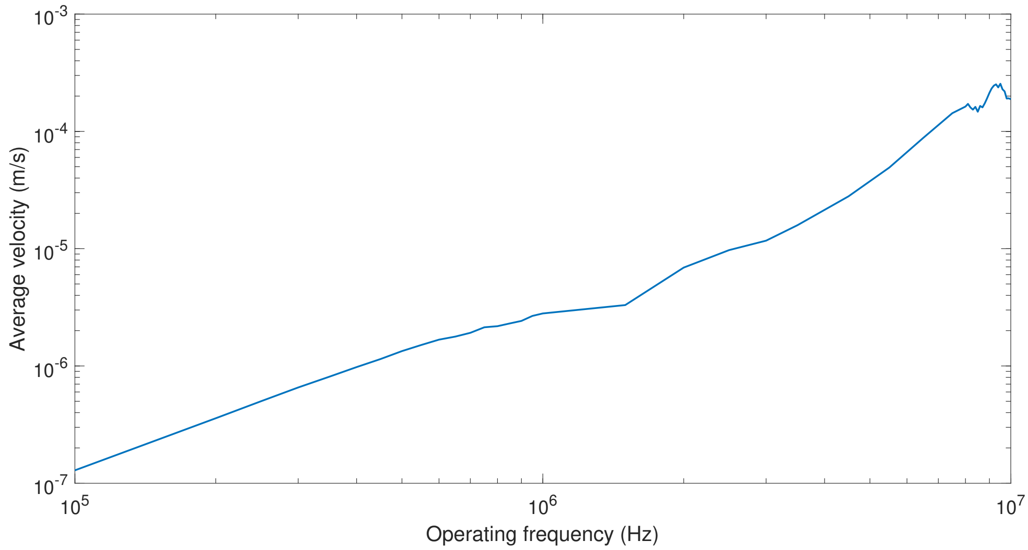


Figure 4.13: The frequency response of a channel with two closed ends and the contribution of PDMS included

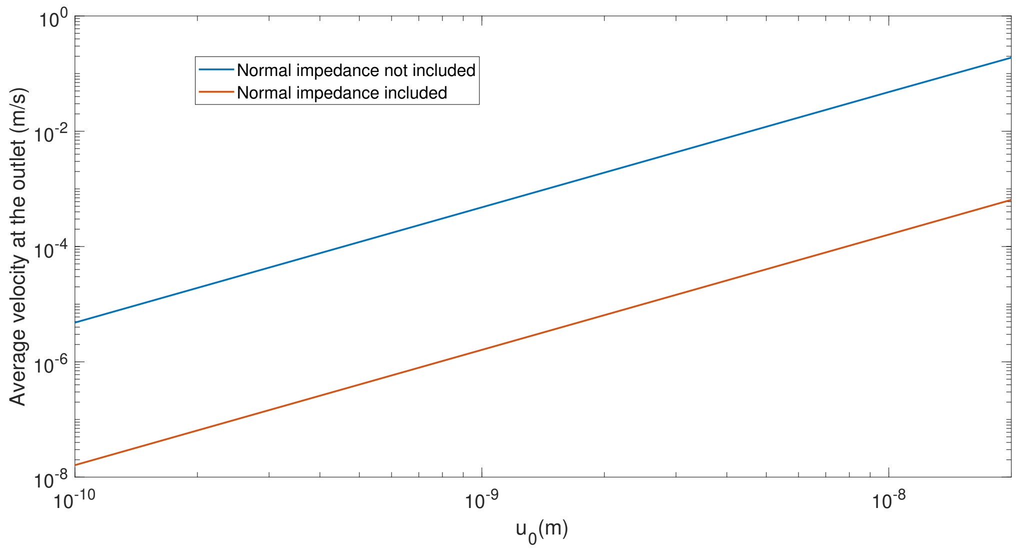


Figure 4.14: The graph shows the relation between $u_0$ and the average velocity at the outlet of the channel when the channel has two closed ends and the frequency is set to the first resonant peak. The blue curve shows the behaviour when PDMS normal impedance is not included, while the red one when it is included.

## 4.2 3D numerical simulations

In this section the feasibility of a 3D model of an acoustic-streaming-based device is investigated. In particular, it is considered the case of a tube with two open ends where the surface acoustic waves propagate perpenducarly to the length of the tube, as displayed in fig. 4.15.

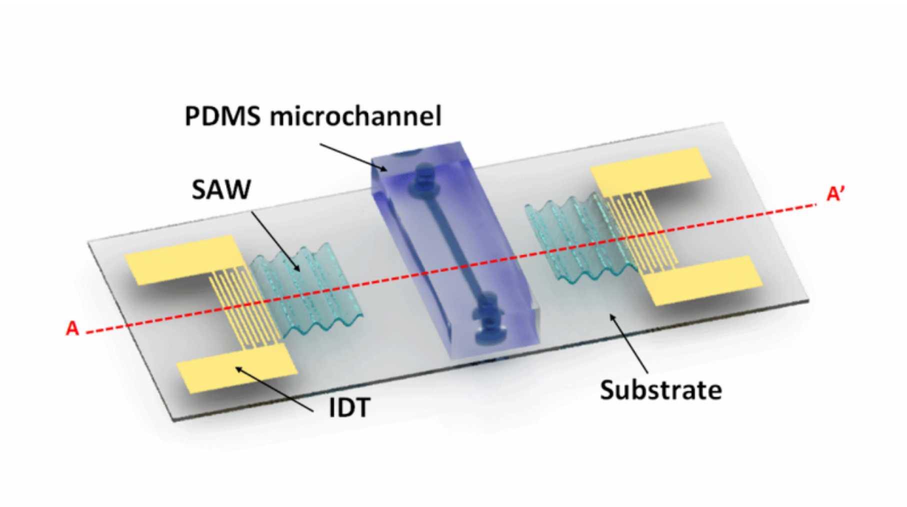


Figure 4.15: Schematic of acoustofluidic device which utilizes surface acoustic waves[54]

There are shown two different ways of triggering acoustic streaming: the first one consists in radiating surface acoustic waves perpendicularly to the propagation direction along all the length of the channel, the second on just along half of it.
Because of computational limits, it is not carried out an analysis as deep as the 2D case. Indeed, the two-dimensional simulations allows are performable for a wide frequency range thanks to the limited required RAM space and computational time, which is not the case of the 3D ones.
Finally the performances of such a pumping mechanism are compared the one based on electrokinetic phenomena.

### 4.2.1 Tube with two open ends

In fig. 4.16 it is pictured the device analysed in this section.


Figure 4.16: Drawing of the tube analyzed in this section. Blue areas represent the *inlet* (left surface) and the *oulet* (right surface) of the channel.

First it is necessary to choose an appropriate value for $n_{el}$, in order for the results of the simulations to be as close as possible to reality.
This simulation investigate the performance at the first resonant frequency (744.5kHz), the pressure at the inlet and the outlet is set to 0, and surface acoustic waves are applied perpendicularly to the propagation direction and all along the length of the channel.
Table 4.3 shows that the value obtained by setting $n_{el}$ to 70 differs from the one resulted from $n_{el} = 90$ by 9.58%: if a tolerance of 10% is considered as in the previous section, it is possible to choose 70 as value for $n_{el}$.

| Number of elements ($n_el$) | Average velocity at the oulet (m/s) |
|---|---|
| 10 | $1.07563 \cdot 10^{-5}$ |
| 30 | $1.23131 \cdot 10^{-5}$ |
| 50 | $1.00982 \cdot 10^{-5}$ |
| 70 | $1.17489 \cdot 10^{-5}$ |
| 90 | $1.06239 \cdot 10^{-5}$ |
| 110 | $9.9515 \cdot 10^{-6}$ |

Table 4.3: Results of the simulation showing how the computed value of the average velocity at the outlet of the tube changes with $n_{el}$ when $u_0$ is set to 1nm

This conclusions are taken in consideration when simulating the case of a 3D tube excited by surface acoustic waves only along the half of the bottom side of the channel too. The average velocity at the outlet results to be

$1.01262 \cdot 10^{-4}$ m/s, so almost one order of magnitude higher than the previous case.
It is fundamental to notice that the leaky behavior - modeled by the attenuation coefficient of eq. 2.24 - is not included in such simulations in order to limit the computational effort.
Fig. 4.17 shows how the average velocity varies with the pressure at the outlet of the channel: the angle coefficient is proved to be $3.3647 \cdot 10^{-4}$m/Pa·s, which is coherent with eq. 1.9 that predicts $3.9488 \cdot 10^{-4}$m/Pa·s (so it results a descrepancy of 14.79%).

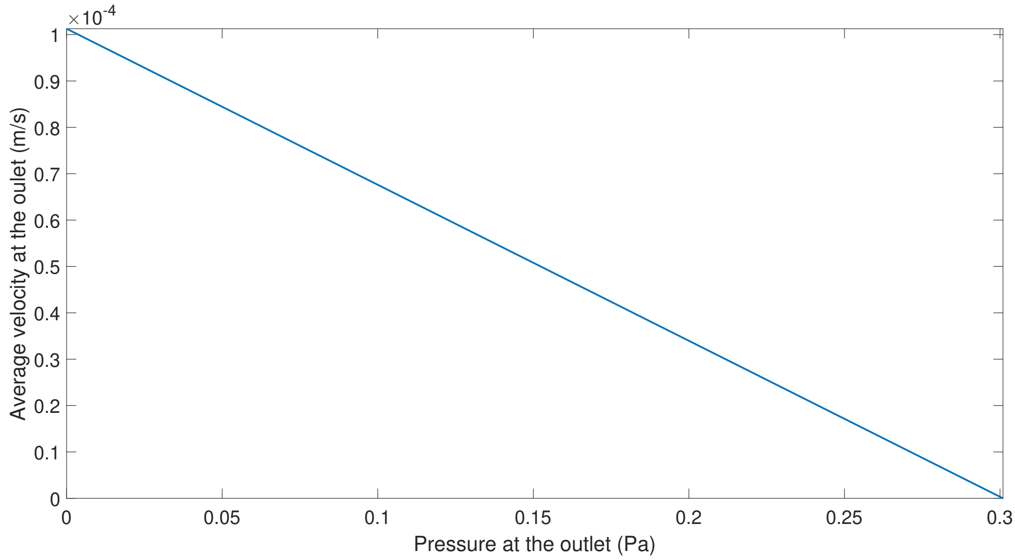


Figure 4.17: Relation between $u_0$ and the average velocity at the outlet of the channel when the channel has two closed ends

A detailed analysis regarding the optimal way of exciting acoustic streaming is not provided in this Master thesis. However, it is clear that the performances of the two study cases presented above differ dramatically:

- when the entire length of the channel is stimulated, two opposite flows are present at the same time in the channel;
- when SAW propagate only along half of it, the flow is uniformly directed towards only one direction.

This difference suggests the second case to be more optimal, and it is confirmed by the resulting average velocity at the outlet (as reported above). Further studies about this aspect could be interesting to be developed in the future.

## 4.3 Comparison with electrokinetic pumps

FEA simulations allow us to establish the relations between the geometrical (i.e. sizes of the tube) and physical (i.e. fluid properties and operating)

parameters and the resulting flow. However, it is difficult to evaluate the performances of such a pumping mechanism by itself: a comparison with another pumping system is necessary.
It is chosen a channel drivven by *electrokinetics*, since it is the most popular among the non-mechanical pumping mechanisms.

### 4.3.1 Electro-osmotic pumps (EOP)

**Electroosmosis** is "the flow of liquid that is in contact with a charged solid surface when an electric field is applied, and it becomes an important consideration with the increased surface area-to-volume ratio associated with microchannels"[55]. Generally surfaces get a finite charge density if put in contact with a water solution: the charged surface attracts counterions[1] and repels coions[2], resulting in the formation of an *electric double layer* (EDL)[56].
As an electric field is applied in parallel with the surface, cations in the EDL region are forced to move in the direction of the electric field. These charged particles drag the liquid, causing a net motion of the bulk fluid known as *electro-osmotic flow* (EOF)[57].

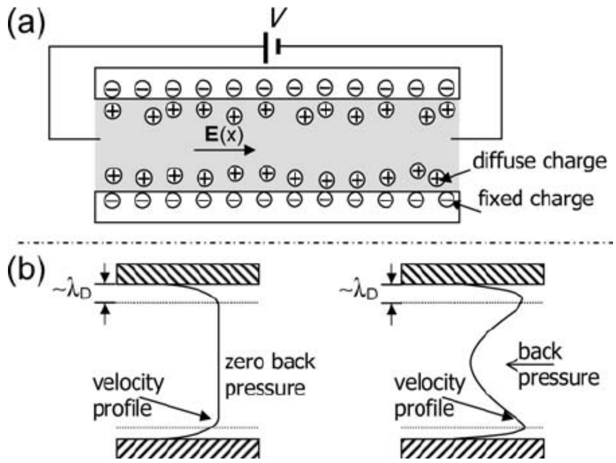


Figure 4.18: Abstract scheme showing the working principle of an electroosmotic pump: (a) $V$ is the applied voltage between the catode and the anode, and *E(x)* the resulting electric field (b)$\lambda_D$ is the Debye length (the distance over which significant charge separation can occur)[58]

Techniques exploiting **boundary effects** result to be quite effective in microfluidics, since the distance separating opposite surfaces is extremely limited [18]: among them, electroosmosis-based pumps are the most pupular. As reported by Squires and Quake[18], the **advantages** associated to this driving mechanism are:

[1]An ion that has the opposite charge to that of another ion within the same solution
[2]An ion that has the same charge to that of another ion within the same solution

- used to pump as well as to separate through electro-osmotic flow (EOF);
- perfectly uniform, straight channels has a flat velocity profile, implying less convective dispersion than for pressure-driven flow;
- no dependence on the tube sizes, in net contrast with pressure-driven flows (as can be seen from eq. 1.9).

Among the **drawbacks**, Squires and Quakes[18] highlight:

- high dependence on chemical properties of the fluid;
- high dependence on walls' charge, which varies with "solution pH, ionic strength, and uncontrollably when solute molecules adsorb onto the walls";
- an inhomogeneous surface charge distribution could affect the resulting flow;
- electrochemical reactions must occur at electrodes in order to maintain an electric field in solution, which give rise to "water electrolysis and its associated bubble formation".

### 4.3.2 Comparison

It is considered a microchannel characterized by the parameters reported in tab. 4.4: the value for $V_{app}$ is chosen so that $u_0$ is 1nm (in case PZT-5H is chosen as piezoelectric material), so the results of the previous simulations are usable to establish a comparison with the electroosmotic driving mechanism.

| Physical entity | Symbol | Value |
|---|---|---|
| Relative permittivity of water | $\epsilon_r$ | 80.2[59] |
| Zeta potential of PDMS | $\zeta_0$ | -83mV[60] |
| Length of the channel | $L$ | 1mm |
| Applied voltage | $V_{app}$ | 14.64mV |

Table 4.4: Parameters of two microchannels actuated by different mechanism: the first one is actuated by EOF, the second one by acoustic streaming

In can proven[18] that for an electroosmotic pump the following equation expresses the velocity along the channel

$$u_{EOF} = \frac{\epsilon_0 \epsilon_r \zeta_0}{\mu L} \cdot V_{app} \tag{4.14}$$

where $\mu$ is the viscosity of the fluid (water in this case), $\epsilon_0$ the vacuum permittivity, $\epsilon_r$ the relative permittivity of the fluid, $L$ the length of the channel, $V_{app}$ the applied voltage and $u_{EOF}$ the velocity along the channel.

By substituting the values reported in tab. 4.4 in eq. 4.14, it results $u_{EOF} = 0.97\mu\text{m/s}$. This value has to be compared with the average normal velocity at the outlet of the channel described in section 4.2.1, with SAW generated only along half of the length of the tube. An average velocity results to be $6.481\mu m/s$, so 6.7 times higher than the EOF counterpart.
It is worth to notice that two contributions have been completely ignored for the acoustic-streaming pump:

- the attenuation provided by PDMS (84.8 $\text{dBcm}^{-1}$[53]) to SAW coming from outside of the channel, which is dependent on the thickness of the wall. If the thickness of the wall is considered to be $600\mu m$[53], the attenuation results 5.088dB. $u_0$ is so reduced by 1.79 times, correspondent to a reduction of 3.23 times for the average velocity at the outlet;

- the leaky behaviour of the SAW propagating at the substrate-water interface, whose effect depends both from the operating frequency and the dimensions of the channel.

# Chapter 5

# Conclusions and future work

This Master thesis has highlighted that:

- a direct comparison between the analithical and FEA models is not straightforward, both for SAW and microfluidic phenomena;
- the height of the piezoelectric substrate ($h_{piezo}$) and the number of IDT pairs influence the generated SAW. It is shown that the resonant frequency reaches a convergent valu as long as $h_{piezo}$ increases;
- the geometrical parameters of microfluidic channels affect the frequency response of the induced acoustic streaming, independently from the applied boundary conditions. In particular it is proven that the optimal working frequencies follow equation 4.8;
- acoustic-streaming-based pumps represent a valid alternative to the traditional driving mechanisms (electroosmotic for example).

Most of the analysis has been dedicated to 2D cases to reduce the computational effort. At the same time it is recognized that 3D analyses cannot be ignored: a real channel allows SAW to be generated perpendicularly to the propagation of the streaming, which cannot be modelled when limiting simulations to a 2D case.
The comparison with the electroosmotic actuation mechanism has clearly signaled a concrete possibility of achieving performances of the same order of magnitude or even higher. Moreover, even if the 3D model does not take into account the leaky behavior of SAW at the solid-fluid interface, the stimulation of acoustic waves from both the sides of the channel should make it not relevant for the analysis.
Since SAW transducers are widely investigated to be integrated in lab-on-chip devices, the author of this document is very confident that this driving mechanism could represent a valid alternative to the traditional counterparts. As a support to previous statement, Ding and Huang[17] report that SAW transducers could be extensevely used for lab-on-chip technology because of their high *biocompatibility*, *fast fluidic actuation*, *simplicity* and *cheapness*, *versatility* and *contact-free manipulation*.

However, it is clear that many topics have not been covered in this document:

- unidirectional SAW-tranducers have not been considered, but they are essential for microfluidics since they improve the performances and maintain the SAW devices at the best operating conditions[9];
- GHz-range has not been investigated for microfluidics, because of the high computational times required (mostly dependent on the necessary size of the finite elemets);
- PDMS influence requires a mathematical study in order to fully comprehend its role in the frequency response of the streaming;
- 3D simulations are limited by computational limits. A more realistic model would also require the inclusion of a vertical tube to inlet water (as displayed in fig. 5.1), but a simpler tube has been chosen to better compare its performances with a the electroosmotic actuation;

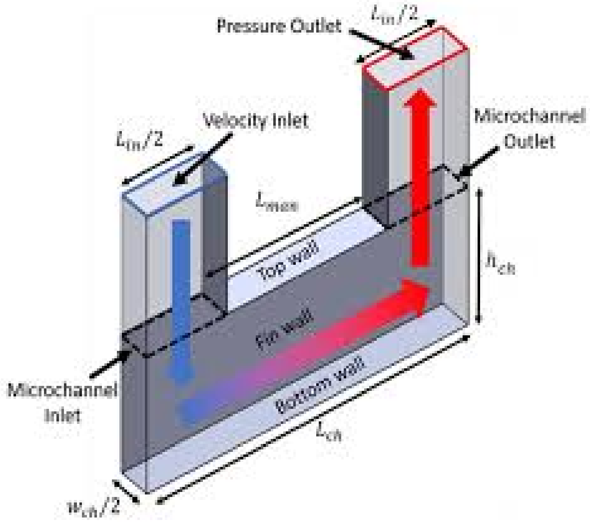


Figure 5.1: Conceptual drawing of a realistic microchannel[61]

- a complete model, including both electro-mechanical coupling and acoustophoretic effect, would be closer to a real device;
- acoustic streaming has been studied when actuated by SAW, but the possibility of using PMUT-based transducers remains an open candidate for novel acoustic-streaming-based devices. It is clear that parameters like the size of the diaphragm, the number of the involved devices and their location in the channel are only a few of the aspects that should be taken into account when designing such a device.

The general remark is that a CFD (Computational Fluid Dynamics) background is necessary when dealing with this topic: the possibility of minimizing the computational time, without renouncing to the quality of the simulation, results to be fundamental to realize a FEA model as close as possible to the reality.

# Chapter 6

# Acknowledgements

I am extremely grateful to Dr. Veronique Rochus, Eng. Billen Margo and Eng. Jones Ben for their constant supervisioning of my work: every-two-weeks meetings allowed to fix the route of my work and complete it in the best way as possible. I would like to thank Prof. Ricciardi Carlo for his support to my Master thesis.

As most of my colleagues, this six months have been affected by the greatest pandemy of the last century: nobody would have ever imagined that such a dramatic event could have impacted our lives. However, I desire to thank imec emergency staff for their work during Covid-19 pandemy: they have guided the company through these difficult months, providing precise information to prevent the increase of cases within imec.

I need to thank all my colleagues with whom I have shared my life in imec: they made going to imec not only a job, but also an amazing life experience.

I feel that these months could not be same, if I would have not met amazing people that turned this period into a joy of life: working on my project was easier because of their continous source of happiness.

Finally, I have to thank my family for the enourmous support they provided me during my University years. I would have never reached my Bachelor and Master results without them: even if they are quoted as last, they are the first I dedicate my thesis to.

# Bibliography


[1] J. Wu, "Acoustic streaming and its applications," *Fluids*, vol. 3, no. 4, p. 108, 2018.

[2] D. W. Dissanayake, S. Al-Sarawi, and D. Abbott, "Surface acoustic wave based wireless mems actuators for biomedical applications," *Acoustic Waves*, p. 181, 2010.

[3] R. White and F. Voltmer, "Direct piezoelectric coupling to surface elastic waves," *Applied physics letters*, vol. 7, no. 12, pp. 314–316, 1965.

[4] M.-I. Rocha-Gaso, C. March-Iborra, Á. Montoya-Baides, and A. Arnau-Vives, "Surface generated acoustic wave biosensors for the detection of pathogens: A review," *Sensors*, vol. 9, no. 7, pp. 5740–5769, 2009.

[5] A. V. Mamishev, K. Sundara-Rajan, F. Yang, Y. Du, and M. Zahn, "Interdigital sensors and transducers," *Proceedings of the IEEE*, vol. 92, no. 5, pp. 808–845, 2004.

[6] J. W. Grate, S. J. Martin, and R. M. White, "Acoustic wave microsensors," *analytical Chemistry*, vol. 65, no. 21, pp. 940A–948A, 1993.

[7] S. Pant, J. Laliberte, and M. Martinez, "Structural health monitoring (shm) of composite aerospace structures using lamb waves," 2013.

[8] A. F. Bower, *Applied mechanics of solids.* CRC press, 2009.

[9] Y. Q. Fu, J. Luo, N.-T. Nguyen, A. Walton, A. J. Flewitt, X.-T. Zu, Y. Li, G. McHale, A. Matthews, E. Iborra, *et al.*, "Advances in piezoelectric thin films for acoustic biosensors, acoustofluidics and lab-on-chip applications," *Progress in Materials Science*, vol. 89, pp. 31–91, 2017.

[10] K. G. E. M. KHAIR, "Subsurface delineation and cavity investigation using geophysical methods in gua musang, kelantan, malaysia," 2016.

[11] M. Tanaka and H. D. Bui, *Inverse Problems in Engineering Mechanics: IUTAM Symposium Tokyo, 1992.* Springer Science & Business Media, 2013.

[12] G. Farnell and E. Adler, "Physical acoustics: Principles and methods: Elastic wave propagation in thin layers vol 9 (new york: Academic)," 1972.

[13] M. Gedge and M. Hill, "Theory of surface acoustic wave devices for particle manipulation," in *Microscale Acoustofluidics*, pp. 337–353, Royal Society of Chemistry, 2014.

[14] J. Friend and L. Y. Yeo, "Microscale acoustofluidics: Microfluidics driven via acoustics and ultrasonics," *Reviews of Modern Physics*, vol. 83, no. 2, p. 647, 2011.

[15] B. C. Saw, *Single-phase unidirectional transducers for low-loss surface acoustic wave devices*. PhD thesis, 1988.

[16] J. W. Strutt, "I. on the circulation of air observed in kundt's tubes, and on some allied acoustical problems," *Philosophical Transactions of the Royal Society of London*, no. 175, pp. 1–21, 1884.

[17] X. Ding, P. Li, S.-C. S. Lin, Z. S. Stratton, N. Nama, F. Guo, D. Slotcavage, X. Mao, J. Shi, F. Costanzo, *et al.*, "Lab-on-a-chip technologies enabled by surface acoustic waves," in *Microscale Acoustofluidics*, pp. 354–398, 2014.

[18] T. M. Squires and S. R. Quake, "Microfluidics: Fluid physics at the nanoliter scale," *Reviews of modern physics*, vol. 77, no. 3, p. 977, 2005.

[19] T. E. Faber, *Fluid dynamics for physicists*. Cambridge university press, 1995.

[20] A. Estupiñán, R. Ortiz, Á. Duarte, J. Sanchez, and J. Arciniegas, "Experimental and numerical study for the representation of standing waves in a kundt's tube," *arXiv preprint arXiv:1812.04365*, 2018.

[21] K. Latifi, H. Wijaya, and Q. Zhou, "Motion of heavy particles on a submerged chladni plate," *Physical Review Letters*, vol. 122, no. 18, p. 184301, 2019.

[22] Wikipedia contributors, "Acoustic streaming — Wikipedia, the free encyclopedia," 2020. [Online; accessed 24-August-2020].

[23] D. N. Lapedes, *McGraw-Hill dictionary of scientific and technical terms*. 1974.

[24] M. Wiklund, R. Green, and M. Ohlin, "Acoustofluidics 14: Applications of acoustic streaming in microfluidic devices," *Lab on a Chip*, vol. 12, no. 14, pp. 2438–2451, 2012.

[25] S. A. Elder, "Cavitation microstreaming," *The Journal of the Acoustical Society of America*, vol. 31, no. 1, pp. 54–64, 1959.

[26] D. Ahmed, X. Mao, J. Shi, B. K. Juluri, and T. J. Huang, "A millisecond micromixer via single-bubble-based acoustic streaming," *Lab on a Chip*, vol. 9, no. 18, pp. 2738–2741, 2009.

[27] K. Sritharan, C. Strobl, M. Schneider, A. Wixforth, and Z. v. Guttenberg, "Acoustic mixing at low reynold's numbers," *Applied Physics Letters*, vol. 88, no. 5, p. 054102, 2006.

[28] T. A. Franke and A. Wixforth, "Microfluidics for miniaturized laboratories on a chip," *ChemPhysChem*, vol. 9, no. 15, pp. 2140–2156, 2008.

[29] R. Rimsa, A. Smith, C. Wälti, and C. Wood, "A planar surface acoustic wave micropump for closed-loop microfluidics," *Applied Physics Letters*, vol. 111, no. 23, p. 234102, 2017.

[30] N.-T. Nguyen, X. Huang, and T. K. Chuan, "Mems-micropumps: a review," *J. Fluids Eng.*, vol. 124, no. 2, pp. 384–392, 2002.

[31] S. Mohith, P. N. Karanth, and S. Kulkarni, "Recent trends in mechanical micropumps and their applications: A review," *Mechatronics*, vol. 60, pp. 34–55, 2019.

[32] L. Schmid, A. Wixforth, D. A. Weitz, and T. Franke, "Novel surface acoustic wave (saw)-driven closed pdms flow chamber," *Microfluidics and nanofluidics*, vol. 12, no. 1-4, pp. 229–235, 2012.

[33] H. Kusumaatmaja, C. Pooley, S. Girardo, D. Pisignano, and J. Yeomans, "Capillary filling in patterned channels," *Physical Review E*, vol. 77, no. 6, p. 067301, 2008.

[34] "Piezoelectricity design notes." `https://www.electroschematics.com/piezoelectricity-design-notes-4/`.

[35] M. E. Gurtin, *An introduction to continuum mechanics*, p. 44. 1982.

[36] D. Dissanayake, *Acoustic Waves*. BoD–Books on Demand, 2010.

[37] V. IA, "Rayleigh and lamb waves, physical theory and applications," *Moscow: Acoustics Institute, Academy of Science of the USSR*, 1967.

[38] Wikipedia contributors, "Advection — Wikipedia, the free encyclopedia," 2020. [Online; accessed 24-August-2020].

[39] N. Nama, R. Barnkob, Z. Mao, C. J. Kähler, F. Costanzo, and T. J. Huang, "Numerical study of acoustophoretic motion of particles in a pdms microchannel driven by surface acoustic waves," *Lab on a Chip*, vol. 15, no. 12, pp. 2700–2709, 2015.

[40] W. L. Nyborg, "Acoustic streaming near a boundary," *The Journal of the Acoustical Society of America*, vol. 30, no. 4, pp. 329–339, 1958.

[41] X. Ding, P. Li, S.-C. S. Lin, Z. S. Stratton, N. Nama, F. Guo, D. Slotcavage, X. Mao, J. Shi, F. Costanzo, *et al.*, "Surface acoustic wave microfluidics," *Lab on a Chip*, vol. 13, no. 18, pp. 3626–3649, 2013.

[42] P. B. Muller, R. Barnkob, M. J. H. Jensen, and H. Bruus, "A numerical study of microparticle acoustophoresis driven by acoustic radiation forces and streaming-induced drag forces," *Lab on a Chip*, vol. 12, no. 22, pp. 4617–4627, 2012.

[43] G. S. Gupta, *Smart sensors and sensing technology*, vol. 20. Springer Science & Business Media, 2008.

[44] S. G. Johnson, "Notes on perfectly matched layers (pmls)," *Lecture notes, Massachusetts Institute of Technology, Massachusetts*, vol. 29, 2008.

[45] J.-P. Berenger *et al.*, "A perfectly matched layer for the absorption of electromagnetic waves," *Journal of computational physics*, vol. 114, no. 2, pp. 185–200, 1994.

[46] W. C. Chew and Q. Liu, "Perfectly matched layers for elastodynamics: a new absorbing boundary condition," *Journal of Computational Acoustics*, vol. 4, no. 04, pp. 341–359, 1996.

[47] K. Uchino and S. Hirose, "Loss mechanisms in piezoelectrics: how to measure different losses separately," *IEEE Transactions on Ultrasonics, ferroelectrics, and frequency control*, vol. 48, no. 1, pp. 307–321, 2001.

[48] M. W. Nygren, "Finite element modeling of piezoelectric ultrasonic transducers," Master's thesis, Institutt for elektronikk og telekommunikasjon, 2011.

[49] C. Chen, S. P. Zhang, Z. Mao, N. Nama, Y. Gu, P.-H. Huang, Y. Jing, X. Guo, F. Costanzo, and T. J. Huang, "Three-dimensional numerical simulation and experimental investigation of boundary-driven streaming in surface acoustic wave microfluidics," *Lab on a Chip*, vol. 18, no. 23, pp. 3645–3654, 2018.

[50] T. Dung Luong and N. Trung Nguyen, "Surface acoustic wave driven microfluidics-a review," *Micro and Nanosystems*, vol. 2, no. 3, pp. 217–225, 2010.

[51] N. R. Skov and H. Bruus, "Modeling of microdevices for saw-based acoustophoresis—a study of boundary conditions," *Micromachines*, vol. 7, no. 10, p. 182, 2016.

[52] "Acoustic streaming in a microchannel cross section." https://www.comsol.it/model/acoustic-streaming-in-a-microchannel-cross-section-17087. Application ID: 17087.

[53] Z. Ni, C. Yin, G. Xu, L. Xie, J. Huang, S. Liu, J. Tu, X. Guo, and D. Zhang, "Modelling of saw-pdms acoustofluidics: physical fields and particle motions influenced by different descriptions of the pdms domain," *Lab on a Chip*, vol. 19, no. 16, pp. 2728–2740, 2019.

[54] Mechanobiology and soft material laboratory, "Acoustofluidics for particle manipulation."

[55] Y. Picó, *Chemical analysis of food: Techniques and applications.* Academic Press, 2012.

[56] M. Rezaei, A. Azimian, and D. T. Semiromi, "The surface charge density effect on the electro-osmotic flow in a nanochannel: a molecular dynamics study," *Heat and Mass Transfer*, vol. 51, no. 5, pp. 661–670, 2015.

[57] X. Wang, C. Cheng, S. Wang, and S. Liu, "Electroosmotic pumps and their applications in microfluidic systems," *Microfluidics and Nanofluidics*, vol. 6, no. 2, pp. 145–162, 2009.

[58] A. Ramos, "Electrohydrodynamic and magnetohydrodynamic micropumps," in *Microfluidic technologies for miniaturized analysis systems*, pp. 59–116, Springer, 2007.

[59] D. G. Archer and P. Wang, "The dielectric constant of water and debye-hückel limiting law slopes," *Journal of physical and chemical reference data*, vol. 19, no. 2, pp. 371–411, 1990.

[60] Z. Liu, Y. Song, and D. Li, "Detecting zeta potential of polydimethylsiloxane (pdms) in electrolyte solutions with atomic force microscope," *Journal of Colloid and Interface Science*, 2020.

[61] S. U. Yuruker, R. K. Mandel, A. Shooshtari, and M. M. Ohadi, "A metamodeling approach for optimization of manifold microchannel systems for high heat flux cooling applications," in *2019 18th IEEE Intersociety Conference on Thermal and Thermomechanical Phenomena in Electronic Systems (ITherm)*, pp. 982–990, IEEE, 2019.

# Appendices

# Appendix A

# Notations

In chapter 2, several vector notations are introduced.
First it is necessary to specify that pedices 1, 2 and 3 indicate x, y and z-direction respectively.
$\boldsymbol{u}$, $\boldsymbol{E}$ and $\boldsymbol{D}$ indicate the displacement, the electric field and the electric displacement field vectors respectively. In particular eq. A.1 show their extended form.

$$\boldsymbol{u} = \begin{pmatrix} u_1 \\ u_2 \\ u_3 \end{pmatrix} \quad \boldsymbol{E} = \begin{pmatrix} E_1 \\ E_2 \\ E_3 \end{pmatrix} \quad \boldsymbol{D} = \begin{pmatrix} D_1 \\ D_2 \\ D_3 \end{pmatrix} \tag{A.1}$$

$\boldsymbol{T}$, $\boldsymbol{S}$ and $\boldsymbol{\epsilon}$ stand for Cauchy stress, strain and dielectric $2^{nd}$-rank tensors, $\boldsymbol{e}$ the $3^{rd}$-rank piezoelectric-coupling tensor, $\boldsymbol{c}$ the $4^{th}$-rank elasticity tensor. In this document, Voigt notation is used: since Cauchy stress tensor is simmetric, a six-dimensional vector both for stress and strain can be generated. According to Voigt-Kelvin notation

$$\begin{cases} 11 \rightarrow 1 \\ 22 \rightarrow 2 \\ 33 \rightarrow 3 \\ 23 \rightarrow 4 \\ 31 \rightarrow 5 \\ 12 \rightarrow 6 \end{cases} \tag{A.2}$$

$$\mathbb{T} = \begin{pmatrix} T_1 \\ T_2 \\ T_3 \\ T_4 \\ T_5 \\ T_6 \end{pmatrix} \quad \mathbb{S} = \begin{pmatrix} S_1 \\ S_2 \\ S_3 \\ S_4 \\ S_5 \\ S_6 \end{pmatrix} \tag{A.3}$$

| Physical entity | Symbol | Expression |
|---|---|---|
| $1^{st}$ Lame' parameter | $\lambda$ | $c_{12}$ |
| $2^{nd}$ Lame' parameter | $\mu$ | $\frac{c_{11}-c_{12}}{2}$ |
| Bulk modulus | K | $\lambda + \frac{2}{3}\mu$ |
| Shear modulus | G | $\mu$ |
| Poisson ratio | $\nu$ | $\frac{\lambda}{3K-\lambda}$ |
| Propagation velocity | $c_{SAW}$ | $\approx \sqrt{\frac{\mu}{\rho}}$ |

Table A.1: Main parameters regarding piezoelectricity

$$\overline{\overline{c^E}} = \begin{pmatrix} c_{11}^E & c_{12}^E & c_{13}^E & c_{14}^E & 0 & 0 \\ c_{12}^E & c_{22}^E & c_{23}^E & c_{24}^E & 0 & 0 \\ c_{13}^E & c_{23}^E & c_{33}^E & c_{34}^E & 0 & 0 \\ c_{14}^E & c_{24}^E & c_{34}^E & c_{44}^E & 0 & 0 \\ 0 & 0 & 0 & 0 & c_{55}^E & 0 \\ 0 & 0 & 0 & 0 & 0 & c_{66}^E \end{pmatrix} \tag{A.4}$$

$$\overline{\overline{s^E}} = \mathrm{inv}(\overline{\overline{c^E}}) \tag{A.5}$$

$$\overline{\overline{\epsilon}} = \begin{pmatrix} \epsilon_{11} & 0 & 0 \\ 0 & \epsilon_{22} & 0 \\ 0 & 0 & \epsilon_{33} \end{pmatrix} \tag{A.6}$$

$$\overline{\overline{e}} = \begin{pmatrix} 0 & e_{12} & e_{13} \\ 0 & e_{22} & e_{23} \\ 0 & e_{32} & e_{33} \\ 0 & e_{42} & e_{43} \\ e_{51} & 0 & 0 \\ e_{61} & 0 & 0 \end{pmatrix} \tag{A.7}$$

$$\overline{\overline{d}} = \overline{\overline{e}} \cdot \overline{\overline{s^E}} \tag{A.8}$$

In chapter 2 it is introduced the matrix element $c_{ijkl}$: in order to make a correct interpretation, it is necessary to split "ij" from and "kl", and use associations A.2 to map each couple.
The same for matrix element $e_{ijk}$, which has to be read by splitting "ij" (mapped by using Voigt notation) and "k". Table A.1 reports the main physical parameters involved for SAW mathematical discussion.

# Appendix B

# Material properties

## B.1 PZT-5H

$$\rho = 7500 kg/m^3 \tag{B.1}$$

$$\overline{\overline{c^E}} = \begin{pmatrix} 127.2 & 80.21 & 84.67 & 0 & 0 & 0 \\ 80.21 & 127.2 & 84.67 & 0 & 0 & 0 \\ 84.67 & 84.67 & 117.43 & 0 & 0 & 0 \\ 0 & 0 & 0 & 22.98 & 0 & 0 \\ 0 & 0 & 0 & 0 & 22.98 & 0 \\ 0 & 0 & 0 & 0 & 0 & 23.47 \end{pmatrix} N/m \tag{B.2}$$

$$\overline{\overline{\epsilon}} = \begin{pmatrix} 1704.4 & 0 & 0 \\ 0 & 1704.4 & 0 \\ 0 & 0 & 1433.6 \end{pmatrix} \tag{B.3}$$

$$\overline{\overline{e}} = \begin{pmatrix} 0 & 0 & -6.62 \\ 0 & 0 & -6.62 \\ 0 & 0 & 23.24 \\ 0 & 17.03 & 0 \\ 17.03 & 0 & 0 \\ 0 & 0 & 0 \end{pmatrix} \tag{B.4}$$

## B.2 Water

| Physical entity | Symbol | Expression | Unit of measurement |
|---|---|---|---|
| Density | $\rho_0$ | 1000 | $kg \cdot m^{-3}$ |
| Shear viscosity | $\mu$ | $8.9 \cdot 10^{-4}$ | $Pa \cdot s$ |
| Bulk viscosity | $\mu_b$ | $2.4 \cdot 10^{-6}$ | $Pa \cdot s$ |
| Propagation velocity | $c_0$ | 1498 | $m \cdot s^{-1}$ |
| Ratio of specific heats | $\gamma$ | 1.012 | 1 |
| Heat capacity at constant pressure | $C_p$ | 4180 | $J \cdot kg^{-1} \cdot K^{-1}$ |
| Compressibility of the fluid | $\chi$ | $4.45 \cdot 10^{-10}$ | $Pa^{-1}$ |
| Thermal conductivity | $k$ | 0.61 | $W \cdot m^{-1} \cdot K^{-1}$ |

# Appendix C

# Rayleigh solution of Navier-Stokes equations

In his article *On the Circulation of Air Observed in Kundt's Tubes, and on some allied acoustical problems*, Lord Rayleigh provided a mathematical description of a steady-state flow caused by a vibratory motion.

## C.1 General formulation

Navier-Stokes equation for momentum is taken into account and developed in Cartesian coordinates (eq. C.2)

$$\frac{\partial \boldsymbol{u}}{\partial t} = -\frac{1}{\rho}\nabla p + \nu\nabla^2\boldsymbol{u} - (\boldsymbol{u}\cdot\nabla)\boldsymbol{u} \tag{C.1}$$

$$\begin{cases} \frac{\partial u_x}{\partial t} = -\frac{1}{\rho}\frac{\partial p}{\partial x} + \nu\nabla^2 u_x - u_x\frac{\partial u_x}{\partial x} - u_y\frac{\partial u_x}{\partial y} \\ \frac{\partial u_y}{\partial t} = -\frac{1}{\rho}\frac{\partial p}{\partial y} + \nu\nabla^2 u_y - u_x\frac{\partial u_y}{\partial x} - u_y\frac{\partial u_y}{\partial y} \end{cases} \tag{C.2}$$

where $\nu$ is the dynamic viscosity, $\rho$ is the density of the fluid, $\boldsymbol{u}$ the velocity field and $p$ the pressure.
In order not to involve $p$ in eq. C.2, both the members of the first equation are derived by $y$, and the ones of the second equation by $x$

$$\nu\nabla^2\left(\frac{\partial u_x}{\partial y}-\frac{\partial u_y}{\partial x}\right)-\frac{\partial}{\partial t}\left(\frac{\partial u_x}{\partial y}-\frac{\partial u_y}{x}\right) = \frac{\partial}{\partial y}\left(u_x\frac{\partial u_x}{\partial x}+u_y\frac{\partial u_x}{\partial y}\right)-\frac{\partial}{\partial x}\left(u_x\frac{\partial u_y}{\partial x}+u_y\frac{\partial u_y}{\partial y}\right) \tag{C.3}$$

By introducing scalar function $\psi$ satisfying conditions C.4

$$u_x = \frac{\partial \psi}{\partial y} \qquad u_y = -\frac{\partial \psi}{\partial x} \tag{C.4}$$

eq. C.3 is rewritable as

$$\nabla^4\psi - \frac{1}{\nu}\frac{\partial}{\partial t}\nabla^2\psi = \frac{u_x}{\nu}\frac{\partial\nabla^2\psi}{\partial x} + \frac{u_y}{\nu}\frac{\partial\nabla^2\psi}{\partial y} \tag{C.5}$$

In a first approximation the right-hand term is neglected since it is of the second order in the velocities

$$\nabla^2\left(\nabla^2 - \frac{1}{\nu}\frac{\partial}{\partial t}\right)\psi \;=\; 0 \tag{C.6}$$

The solution of eq. C.6 is supposed to have an harmonic behaviour - and so to be proportional to $e^{i\omega t}cos(kx)$ - and being writeable as a linear combination of two wave-functions $\psi_1$ and $\psi_2$ such that

$$\nabla^2\psi_1 \;=\; \left(\frac{\partial^2}{\partial y^2} - k^2\right)\psi_1 \;=\; 0 \tag{C.7}$$

$$\left(\nabla^2 - \frac{1}{\nu}\frac{\partial}{\partial t}\right)\psi_2 \;=\; \left(\frac{\partial^2}{\partial y^2} - k^2 - \frac{i}{\nu}\omega\right)\psi_2 \;=\; \left(\frac{\partial^2}{\partial y^2} - k'^2\right)\psi_1 \;=\; 0 \tag{C.8}$$

$$\begin{cases}\psi_1 \;=\; A_1e^{-ky} + A_2e^{ky}\\ \psi_2 \;=\; B_1e^{-k'y} + B_2e^{k'y}\end{cases} \tag{C.9}$$

Since $\frac{\omega}{\nu}$ is generally very high, it is possible to make the following approximation

$$k' \;\approx\; \sqrt{\frac{\omega}{2\nu}}(1+i) \;=\; \beta(1+i) \tag{C.10}$$

In order to assign proper boundary condition, in the following section a study case is analysed: it has been chosen the one of a vessel whose horizontal bottom occupies a fixed plane at $y = 0$ ($y$ is measured upwards).

## C.2 Vessel with a closed bottom side

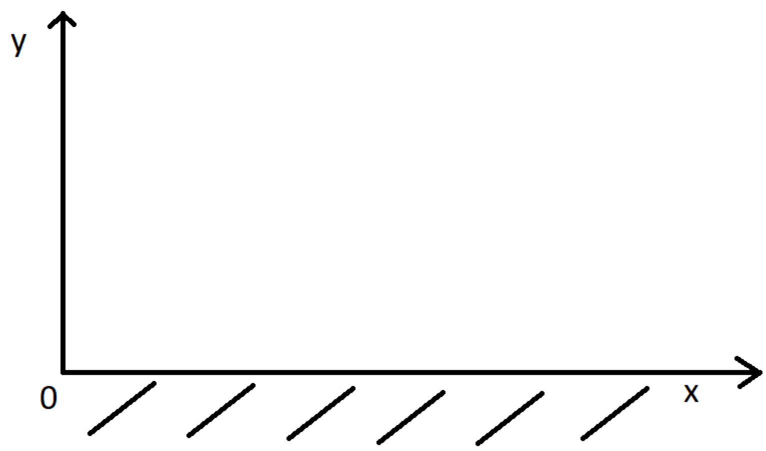


Figure C.1: Maximum vertical displacement of the free surface by varying the number of IDT pairs

### C.2.1 Boundary conditions

If no other solids are present in the neighbourhood of the bottom, it is possible to suppose $B_2 = 0$, and so

$$\begin{cases} \psi(0) \;=\; \psi_1(0)+\psi_2(0) \;=\; A_1+A_2+B_1 \;=\; 0 \\ \frac{\partial\psi}{\partial y}(0) \;=\; \frac{\partial\psi_1}{\partial y}(0)+\frac{\partial\psi_2}{\partial y}(0) \;=\; -kA_1+kA_2-k'B_1 \;=\; 0 \end{cases} \tag{C.11}$$

By substituting eq. C.11 into eq. C.9, $\psi$ is writeable as

$$\psi \;=\; B_1\left(-\cosh ky+\frac{k'}{k}\sinh ky+e^{-k'y}\right) \tag{C.12}$$

If the region close to bottom boundary is taken into account, and the imaginary are neglected, eq. C.12 allows to write $u_x$ and $u_y$ as

$$\begin{cases} u_x \;=\; u_0\cos kx[-\frac{k\sinh ky}{\beta\sqrt{2}}\cos(\omega t-\frac{\pi}{4})+\cosh ky\cos\omega t-e^{-\beta y}\cos(\omega t-\beta y)] \\ u_y \;=\; u_0\sin kx[-\frac{k\cosh ky}{\beta\sqrt{2}}\cos(\omega t-\frac{\pi}{4})+\sinh ky\cos\omega t+\frac{ke^{-\beta y}}{\beta\sqrt{2}}\cos(\omega t-\frac{\pi}{4}-\beta y)] \end{cases} \tag{C.13}$$

Since the final goal is investigating the steady-state motion of the fluid, it is worth to analyse what happens when a particle moves from (x,y) to (x+$\xi$,y+$\eta$): if Taylor expansion is applied, eq. C.14 shows that

$$u_x(x+\xi,y+\eta) \;=\; u_x(x,y)+\frac{\partial u_x}{\partial x}\xi+\frac{\partial u_x}{\partial y}\eta \tag{C.14}$$

with

$$\xi=\int_0^{\Delta t} u_x\,dt \qquad\qquad \eta=\int_0^{\Delta t} u_y\,dt \tag{C.15}$$

Being u(x,y) periodic and $\int \frac{\partial u_x}{\partial x}\xi\,dt=0$, only the second term of eq. C.14 is not negligible and consists of two parts: the first independent of t, and the second harmonic functions of $2\omega t$.
Only the former is considered, since it is non-zero if averaged over time.

$$\overline{u_x} \;=\; \frac{u_0^2\sin 2kxe^{-\beta y}}{4\omega}\left[k\cosh ky\cos\beta y+\sqrt{2}\beta\sinh ky\sin\left(\beta y-\frac{\pi}{4}\right)-ke^{-\beta y}\right] \tag{C.16}$$

Near the bottom boundary the mean velocity results to be

$$\overline{u_x} \;=\; \frac{u_0^2\sin 2kxe^{-\beta y}}{4v}[\cos\beta y+\beta y(\sin\beta y-\cos\beta y)-e^{-\beta y}] \tag{C.17}$$

where $v=\frac{\omega}{k}$ is the phase velocity.

According to eq. C.7 and C.8

$$\nabla^2\psi \;=\; \nabla^2(\psi_1+\psi_2) \;=\; \nabla^2\psi_2 \;=\; \frac{1}{\nu}\frac{\partial\psi_2}{\partial t} \tag{C.18}$$

Since eq. C.13 provides the expressions for $\psi$, $u_x$ and $u_y$, an expression for the right-hand member of eq. C.5 can be calculated as

$$\frac{u_x}{\nu}\frac{\partial \nabla^2\psi}{\partial x} + \frac{u_y}{\nu}\frac{\partial \nabla^2\psi}{\partial y}$$

$$= \frac{\omega k u_0^2 \sin 2kx e^{-\beta y}}{4\nu^2\beta\sqrt{2}}\left[\left(\frac{k}{\beta\sqrt{2}} - \frac{\beta\sqrt{2}}{k}\right)\sinh ky \sin\beta y - \sqrt{2}\cosh ky\cos\beta y + \sqrt{2}e^{-\beta y}\right] \tag{C.19}$$

where the terms in $2\omega t$ are not taken into account.
In close proximity of the bottom boundary

$$\frac{u_x}{\nu}\frac{\partial \nabla^2\psi}{\partial x} + \frac{u_y}{\nu}\frac{\partial \nabla^2\psi}{\partial y} \approx \frac{\omega k u_0^2 \sin 2kx e^{-\beta y}}{4\nu^2\beta}[-\beta y\sin\beta y - \cos\beta y + e^{-\beta y}] \tag{C.20}$$

Since $k << \beta$, it is possible to approximate

$$\nabla^4\psi \approx \frac{d^4}{dy^4}\psi = \frac{u_x}{\nu}\frac{\partial \nabla^2\psi}{\partial x} + \frac{u_y}{\nu}\frac{\partial \nabla^2\psi}{\partial y} \tag{C.21}$$

The solution of the equation resulting from substituting eq. C.20 into eq. C.21 is

$$\psi = \frac{\omega k u_0^2 \sin 2kx e^{-\beta y}}{4\nu^2\beta^5}\left[\frac{3}{4}\cos\beta y + \frac{1}{2}\sin\beta y + \frac{1}{4}\beta y\sin\beta y + \frac{1}{16}e^{-\beta y}\right] \tag{C.22}$$

The complementary function of eq. C.21 may be rewritten as

$$\frac{\omega k u_0^2 \sin 2kx}{4\nu^2\beta^5}[(C+Dy)e^{-2ky} + (C'+D'y)e^{2ky}] = \frac{u_0^2\sin 2kx}{\beta V}(C+Dy)e^{-2ky} \tag{C.23}$$

So $u_x$ results to be

$$u_x = \frac{u_o^2\sin 2kx}{v}\left\{e^{-\beta y}\left[-\sin\beta y - \frac{1}{4}\cos\beta y + \frac{1}{4}\beta y\cos\beta y - \frac{1}{4}\beta y\sin\beta y - \frac{1}{8}e^{-\beta y}\right] + \beta^{-1}e^{-2ky}[D - 2k(D+Cy)]\right\} \tag{C.24}$$

Because of $u_x(y=0)$ and $u_y(y=0)$, it is possible to get

$$C = -\frac{13}{16} \qquad D = \frac{3}{8}\beta \tag{C.25}$$

Thus

$$u_x = \frac{u_o^2\sin 2kx}{V}\left\{e^{-\beta y}\left[-\sin\beta y - \frac{1}{4}\cos\beta y + \frac{1}{4}\beta y\cos\beta y - \frac{1}{4}\beta y\sin\beta y - \frac{1}{8}e^{-\beta y}\right] + \frac{3}{8}e^{-2ky}[1-2ky]\right\} \tag{C.26}$$

Finally it is necessary to sum up the term in eq. C.17

$$u'_x = \frac{u_0^2 \sin 2kx}{V}\left[e^{-\beta y}\left( - \sin \beta y - \frac{3}{8}e^{-\beta y}\right) + \frac{3}{8}e^{-2ky}(1-2ky)\right] \quad (C.27)$$

At the short distance the first term in the brackets becomes negligible, so it is results simply in

$$u'_x = \frac{3}{8}\frac{u_0^2 \sin 2kx}{V}e^{-2ky}(1-2ky) \quad (C.28)$$